Time domain calculation of the electromagnetic self-force on eccentric geodesics in Schwarzschild spacetime

Roland Haas
Theoretical Astrophysics, California Institute of Technology, Pasadena, CA 91125 and
Center for Relativistic Astrophysics, Georgia Institute of Technology, Atlanta, GA 30332
(Dated: December 19, 2011)

I calculate the self-force acting on a particle with electric charge q moving on a generic geodesic around a Schwarzschild black hole. Using methods similar to those developed for the scalar field case discussed in [1], I investigate the relative sizes of the conservative (half-advanced plus half-retarded) and dissipative (half-advanced minus half-retarded) pieces of the self-force. I also display the regularization parameters used in the mode-sum regularization scheme.

PACS numbers: 04.25.-g, 04.40.-b, 41.60.-m, 45.50.-j, 02.60.Cb

I. INTRODUCTION

This is the second paper of a series of papers studying the self-force on a point particle in generic geodesic orbit around a Schwarzschild black hole. I extend the previous calculation of the scalar self-force [2] to electromagnetism, studying in particular the effects of the conservative part of the self-force.

A test particle in orbit around a black hole will follow a geodesic. Going beyond the test mass limit, this is no longer true and the particle's path will deviate from a geodesic of the background spacetime. As seen from the background spacetime, the particle is said to experiences a self-force due to its interaction with its own field. In order to accurately model the motion of the body, including its inspiral toward the black hole, I seek to evaluate the self-force and calculate its effect on the motion. Several methods to achieve this have been proposed in the literature [3–5]. I elect to use the mode-sum regularization scheme introduced by Barack and Ori [3], which been proven to be highly accurate.

In this paper, rather than dealing with the gravitational problem, I focus on the technically simpler problem of a point particle endowed with an electric charge q orbiting a Schwarzschild black hole of mass M. In this context I use a numerical simulation to check the analytically calculated regularization parameters used in the mode-sum regularization scheme, which I calculate in a manner analogous to [2]. This calculation also makes it possible to investigate the behaviour of the conservative (half-advanced plus half-retarded) part of the self-force in the strong-field limit, extending previous work by Pound and Poisson [6]. Different from the scalar case calculation, where the conservative self-force is suppressed, the conservative electromagnetic self-force appears at the same post Newtonian order as the gravitational conservative self-force. Agreement, even if only qualitative, between the results for the electromagnetic problem, where our physical intuition allows us to understand the mechanisms at work, and those for a point mass recently explored by [7, 8] can thus help provide a clearer understanding of the mechanisms at work in the gravitational case as well.

Throughout the paper I use geometrized units in which $G = c = 1$ and the sign conventions of [9].

A. The problem

Since my approach is essentially identical to that described in [2] and [1] (paper I and paper II from now on), I will only briefly introduce the required notation.

The first order self-force is calculated on a geodesic of Schwarzschild spacetime, whose metric is written in Schwarzschild coordinates as

$$\mathrm{d}s^2 = -f\mathrm{d}t^2 + f^{-1}\mathrm{d}r^2 + r^2\mathrm{d}\Omega, \tag{1.1}$$

where $f = \left(1 - \frac{2M}{r}\right)$, $\mathrm{d}\Omega = \left(\mathrm{d}\theta^2 + \sin^2\theta\mathrm{d}\phi^2\right)$ is the metric on a two-sphere, and t, r, θ and ϕ are the usual Schwarzschild coordinates. I numerically solve the Maxwell equations

$$g^{\beta\gamma}\nabla_\gamma F_{\alpha\beta}(x) = 4\pi j_\alpha(x), \tag{1.2}$$

$$\nabla_{[\gamma}F_{\alpha\beta]}(x) = 0, \tag{1.3}$$

$$j_\alpha(x) = q\int_\gamma u_\alpha(\tau)\delta_4\big(x, z(\tau)\big)\mathrm{d}\tau, \tag{1.4}$$

where ∇_α is the covariant derivative compatible with the metric $g_{\alpha\beta}$, $F_{\alpha\beta}$ is the Faraday field tensor sourced by a charge q which moves along a world line $\gamma : \tau \mapsto z(\tau)$ parametrized by proper time τ. The current density $j_\alpha(x)$ appearing on the right-hand side is written in terms of a scalarized four-dimensional Dirac δ-function $\delta_4(x, x') \equiv \delta(x_0 - x'_0)\delta(x_1 - x'_1)\delta(x_2 - x'_2)\delta(x_3 - x'_3)/\sqrt{-\det(g_{\alpha\beta})}$. After having obtained the Faraday tensor I regularize it using the mode-sum regularization scheme introduced by Barack and Ori [3]

$$F^R_{(\mu)(\nu)} = F^{\mathrm{ret}}_{(\mu)(\nu)} - q\sum_\ell \left[A_{(\mu)(\nu)}\left(\ell + \frac{1}{2}\right) + B_{(\mu)(\nu)} + \frac{C_{(\mu)(\nu)}}{\ell + \frac{1}{2}} + \frac{D_{(\mu)(\nu)}}{(\ell - \frac{1}{2})(\ell + \frac{3}{2})} + \cdots\right], \tag{1.5}$$

where indices in parenthesis (μ) signify components with respect to an orthonormal tetrad $e^{\alpha}{}_{(\mu)}$ and the coefficients $A_{(\mu)(\nu)}$, $B_{(\mu)(\nu)}$, $C_{(\mu)(\nu)}$, and $D_{(\mu)(\nu)}$ are independent of ℓ; they are listed in Appendix B. Finally I compute the regularized self-force

$$F^{\rm self}_{\alpha} \equiv q F^{R}_{\alpha\beta} u^{\beta} \tag{1.6}$$

from the regularized Faraday tensor and the four velocity of the particle.

B. Organization of this paper

In Sec. II I introduce the ideas behind the discretization scheme used in the numerical simulation. Sec. III describes the choices I make in order to handle the problems of specifying initial data and proper boundary conditions. In Sec. VII I describe the tests I performed in order to validate my implementation of the numerical method. Sec. VIII contains sample results for a small number of representative simulations. Finally in Sec. IX I calculate the conservative self-force for the same set of simulations. The appendices contain technical details and an alternative calculation using the vector potential instead of the Faraday tensor.

II. NUMERICAL METHOD

In this section I describe the algorithm used to integrate the Maxwell equations numerically. I use the second-order algorithm introduced by Lousto and Price [10] suitably extended to handle a coupled system of equations.

A. Wave equations for the Faraday tensor

I introduce a vector potential A_α in terms of which the Faraday tensor is given by

$$F_{\alpha\beta} = A_{\beta,\alpha} - A_{\alpha,\beta}, \tag{2.1}$$

where a comma denotes an ordinary derivative. I use vector spherical harmonics $Z^{\ell m}_A = \partial_A Y^{\ell m}$ and $X^{\ell m}_A = \epsilon_A{}^B \partial_B Y^{\ell m}$, where ϵ_{AB} is the Levi-Civita tensor associated with the metric Ω_{AB} on the two-sphere ($\epsilon_{\theta\phi} = \sin\theta$), as introduced in [11, 12]. I decompose the vector potential and the current density into

$$A_a(t,r,\theta,\phi) = A^{\ell m}_a(t,r) Y_{\ell m}(\theta,\phi), \tag{2.2a}$$

$$j_a(t,r,\theta,\phi) = j^{\ell m}_a(t,r) Y_{\ell m}(\theta,\phi) \qquad \text{for } a = t, r, \tag{2.2b}$$

$$A_A(t,r,\theta,\phi) = v_{\ell m}(t,r) Z^{\ell m}_A(\theta,\phi) + \tilde{v}_{\ell m}(t,r) X^{\ell m}_A(\theta,\phi), \tag{2.2c}$$

$$j_A(t,r,\theta,\phi) = j^{\rm even}_{\ell m}(t,r) Z^{\ell m}_A(\theta,\phi) + j^{\rm odd}_{\ell m}(t,r) X^{\ell m}_A(\theta,\phi) \quad \text{for } A = \theta, \phi, \tag{2.2d}$$

where a summation over ℓ and m is implied. Substituting these into Eq. (1.2) I arrive at two sets of coupled equations for the even ($A^{\ell m}_a$, $v_{\ell m}$) and odd ($\tilde{v}_{\ell m}$) modes

$$-f\frac{\partial^2 A^{\ell m}_t}{\partial r^2} + f\frac{\partial^2 A^{\ell m}_r}{\partial t \partial r} - \frac{2f}{r}\frac{\partial A^{\ell m}_t}{\partial r} + \frac{2f}{r}\frac{\partial A^{\ell m}_r}{\partial t} - \frac{\ell(\ell+1)}{r^2}\frac{\partial v_{\ell m}}{\partial t} + \frac{\ell(\ell+1)}{r^2} A^{\ell m}_t = 4\pi j^{\ell m}_t, \tag{2.3a}$$

$$f^{-1}\frac{\partial^2 A^{\ell m}_r}{\partial t^2} - f^{-1}\frac{\partial^2 A^{\ell m}_t}{\partial t \partial r} - \frac{\ell(\ell+1)}{r^2}\frac{\partial v_{\ell m}}{\partial r} + \frac{\ell(\ell+1)}{r^2} A^{\ell m}_r = 4\pi j^{\ell m}_r, \tag{2.3b}$$

$$f^{-1}\frac{\partial^2 v_{\ell m}}{\partial t^2} - f\frac{\partial^2 v_{\ell m}}{\partial r^2} - \frac{2M}{r^2}\frac{\partial v_{\ell m}}{\partial r} + f\frac{\partial A^{\ell m}_r}{\partial r} - f^{-1}\frac{\partial A^{\ell m}_t}{\partial t} + \frac{2M}{r^2} A^{\ell m}_r = 4\pi j^{\rm even}_{\ell m}, \tag{2.3c}$$

$$f^{-1}\frac{\partial^2 \tilde{v}_{\ell m}}{\partial t^2} - f\frac{\partial^2 \tilde{v}_{\ell m}}{\partial r^2} - \frac{2M}{r^2}\frac{\partial \tilde{v}_{\ell m}}{\partial r} + \frac{\ell(\ell+1)}{r^2}\tilde{v}_{\ell m} = 4\pi j^{\rm odd}_{\ell m}, \tag{2.3d}$$

where

$$j^{\ell m}_t = -\frac{qf}{r_0^2}\bar{Y}^{\ell m}(\frac{\pi}{2},\varphi_0)\delta(r-r_0), \tag{2.4a}$$

$$j^{\ell m}_r = \frac{q\dot{r}_0}{E r_0^2}\bar{Y}^{\ell m}(\frac{\pi}{2},\varphi_0)\delta(r-r_0), \tag{2.4b}$$

$$j^{\rm even}_{\ell m} = -\frac{imqfJ}{\ell(\ell+1)E r_0^2}\bar{Y}^{\ell m}(\frac{\pi}{2},\varphi_0)\delta(r-r_0), \tag{2.4c}$$

$$j^{\rm odd}_{\ell m} = -\frac{qfJ}{\ell(\ell+1)E r_0^2}\partial_\theta \bar{Y}^{\ell m}(\frac{\pi}{2},\varphi_0)\delta(r-r_0). \tag{2.4d}$$

In the equation above an overbar denotes complex conjugation, an overdot denotes differentiation with respect to τ, $E = -u_t$ is the particle's conserved energy per unit mass, $J = u_\phi$ its conserved angular momentum per unit mass, and $u^\alpha = \frac{{\rm d}z^\alpha}{{\rm d}\tau}$ is its four velocity. Quantities bearing a subscript "0" are evaluated at the particle's position; they are functions of τ that are obtained by solving the geodesic equation

$$u^\beta \nabla_\beta u^\alpha = 0 \tag{2.5}$$

in the background spacetime. Without loss of generality, I have confined the motion of the particle to the equatorial plane $\theta = \frac{\pi}{2}$.

The three even mode equations Eq. (2.3a) – Eq. (2.3c) are not yet amenable to a numerical treatment, as they are highly coupled. In order to obtain a more convenient set of equation I define the auxiliary fields

$$\psi^{\ell m} \equiv -r^2 \left(\frac{\partial A_t^{\ell m}}{\partial r} - \frac{\partial A_r^{\ell m}}{\partial t} \right), \tag{2.6}$$

$$\chi^{\ell m} \equiv f \left(A_r^{\ell m} - \frac{\partial v^{\ell m}}{\partial r} \right), \tag{2.7}$$

$$\xi^{\ell m} \equiv A_t^{\ell m} - \frac{\partial v^{\ell m}}{\partial t}, \tag{2.8}$$

which, up to scaling factors, are just the even multipole moments of the tr, $r\phi$ and $t\phi$ components of the Faraday tensor

$$F_{tr} = \sum_{\ell,m} \frac{\psi^{\ell m}}{r^2} Y^{\ell m}, \tag{2.9}$$

$$F_{tA} = \sum_{\ell,m} (-\xi^{\ell m} Z_A^{\ell m} + \tilde{v}_{,t}^{\ell m} X_A^{\ell m}), \tag{2.10}$$

$$F_{rA} = \sum_{\ell,m} (\frac{\chi^{\ell m}}{f} Z_A^{\ell m} + \tilde{v}_{,r}^{\ell m} X_A^{\ell m}), \tag{2.11}$$

$$\begin{aligned} F_{\theta\varphi} &= \sum_{\ell,m} \tilde{v}_{\ell m} \left(X_{\phi,\theta}^{\ell m} - X_{\theta,\phi}^{\ell m} \right) \\ &= -\sum_{\ell,m} \ell(\ell+1) \tilde{v}_{\ell m} \sin(\theta) Y^{\ell m}. \end{aligned} \tag{2.12}$$

I note that the three fields $\psi^{\ell m}$, $\chi^{\ell m}$ and $\xi^{\ell m}$ are not independent of each other, in fact knowledge of $\psi^{\ell m}$ is sufficient to reconstruct $\chi^{\ell m}$ and $\xi^{\ell m}$. Eq. (2.3a) can be rearranged to yield

$$\xi^{\ell m} = -\frac{f}{\ell(\ell+1)} \frac{\partial \psi^{\ell m}}{\partial r} - \frac{4\pi}{\ell(\ell+1)} j_t^{\ell m}, \tag{2.13}$$

and similarly from Eq. (2.3b)

$$\chi^{\ell m} = -\frac{1}{\ell(\ell+1)} \frac{\partial \psi^{\ell m}}{\partial t} - \frac{4\pi f}{\ell(\ell+1)} j_r^{\ell m}, \tag{2.14}$$

showing that knowledge of $\psi^{\ell m}$ is sufficient to reconstruct the even multipole components of the Faraday tensor. In this work however I choose to solve for $\chi^{\ell m}$ and $\xi^{\ell m}$ directly, rather than to numerically differentiate $\psi^{\ell m}$ to obtain them. The gain in speed from reducing the number of equations does not seem to offset the additional time required to calculate $\psi^{\ell m}$ accurately enough to obtain good approximations for its derivatives at the location of the particle. In this approach Eqs. (2.13) and (2.14) are treated as constraints that the dynamical variables have to satisfy.

Dropping the superscripts ℓ, m for notational convenience and following [13] I form linear combinations of derivatives of Eqs.(2.3a) – (2.3c). I use $[\partial_r(r^2\,(2.3b)) - \partial_t(r^2\,(2.3a))]$ for ψ and find

$$\frac{\partial^2 \psi}{\partial r^{*2}} - \frac{\partial^2 \psi}{\partial t^2} - V\psi = S_\psi, \tag{2.15a}$$

$$S_\psi = 4\pi f \left[\frac{\partial (r^2 j_t^{\ell m})}{\partial r} - \frac{\partial (r^2 j_r^{\ell m})}{\partial t} \right], \tag{2.15b}$$

where $V = \ell(\ell+1)\frac{r-2M}{r^3}$ and $r^* = r + 2M\ln(\frac{r}{2M} - 1)$ is the Regge-Wheeler tortoise coordinate. Similarly I use $[f\,(2.3b) - \partial_r(f\,(2.3c))]$ for χ and $[(2.3a) - \partial_t(2.3c)]$ for ξ. I find

$$\frac{\partial^2 \chi}{\partial r^{*2}} - \frac{\partial^2 \chi}{\partial t^2} - V\chi = S_\chi, \tag{2.15c}$$

$$S_\chi = 4\pi f \left[\frac{\partial (f j_{\ell m}^{\rm even})}{\partial r} - f j_r^{\ell m} \right], \tag{2.15d}$$

$$\frac{\partial^2 \xi}{\partial r^{*2}} - \frac{\partial^2 \xi}{\partial t^2} - V\xi - V_\xi \psi = S_\xi, \tag{2.15e}$$

$$S_\xi = 4\pi f \left[\frac{\partial (f j_{\ell m}^{\rm even})}{\partial t} - f j_t^{\ell m} \right], \tag{2.15f}$$

where $V_\xi = \frac{2(r-3M)(r-2M)}{r^5}$. While still partially coupled Eqs. (2.15b) – (2.15f) are much easier to deal with than the original set Eqs. (2.3a) – (2.3c). The coupling is in the form of a staggering, which allows me to first solve for ψ and use this result in the calculation of ξ. On the other hand, the source terms appearing on the right-hand side contain derivatives of Dirac's δ-function resulting in fields that are discontinuous at the location of the particle. Lousto's scheme is designed to cope with precisely this situation.

I derive explicit expressions for the source terms S_α on the right hand sides

$$S_\alpha = G_\alpha(t) f_0 \delta(r - r_0) + F_\alpha(t) f \delta'(r - r_0), \tag{2.16a}$$

$$G_\psi(t) = -\frac{4\pi q}{E^2} f_0 \left(\ddot{r}_0 - \frac{im\dot{r}_0 J}{r_0^2} \right) \bar{Y}_{\ell m}(\frac{\pi}{2}, \varphi_0), \tag{2.16b}$$

$$F_\psi(t) = 4\pi q f_0 \left(\frac{\dot{r}_0^2}{E^2} - 1 \right) \bar{Y}_{\ell m}(\frac{\pi}{2}, \varphi_0), \tag{2.16c}$$

$$G_\chi(t) = -\frac{4\pi q \dot{r}_0}{E r_0^2} f_0 \bar{Y}_{\ell m}(\frac{\pi}{2}, \varphi_0), \tag{2.16d}$$

$$F_\chi(t) = -\frac{4\pi q J i m}{E\ell(\ell+1) r_0^2} f_0^2 \bar{Y}_{\ell m}(\frac{\pi}{2}, \varphi_0), \tag{2.16e}$$

$$\begin{aligned} G_\xi(t) = -4\pi q \Bigg\{ &\frac{Jim}{E^2 \ell(\ell+1) r_0^2} \left[\left(\frac{2M}{r_0^2} - \frac{2f_0}{r_0} \right) \dot{r}_0 \right. \\ &\left. - \frac{imJ}{r_0^2} \right] - \frac{1}{r_0^2} \Bigg\} f_0 \bar{Y}_{\ell m}(\frac{\pi}{2}, \varphi_0), \end{aligned}$$

$$F_\xi(t) = \frac{4\pi q J i m \dot{r}_0}{E^2 \ell(\ell+1) r_0^2} f_0^2 \bar{Y}_{\ell m}(\frac{\pi}{2}, \varphi_0). \tag{2.16f}$$

My functions G_α and F_α correspond to G/f_0 and F/f in [10], respectively, they are independent of r (but do contain terms in $r_0(t)$). I prefer this form of the source

terms over the form given in [10] since it simplifies the integral over the source term Eq. (3.6) of [10]

$$\iint \mathrm{d}AS = 2\int_{t_1}^{t_2}\left[\frac{G(r_0(t),t)}{1-2M/r_0(t)} - \frac{\partial}{\partial r}\left(\frac{F(r,t)}{1-2M/r}\right)\Big|_{r=r_0(t)}\right]\mathrm{d}t \pm 2\frac{F(r_0(t_1),t_1)}{[1-2M/r_0(t_1)]^2}[1\mp \dot{r}_0^*(t_1)]^{-1} \pm 2\frac{F(r_0(t_2),t_2)}{[1-2M/r_0(t_2)]^2}[1\pm \dot{r}_0^*(t_2)]^{-1}. \quad (2.17)$$

Since $G^{\rm Lousto} = f_0 G_\alpha(t)$ and $G^{\rm Lousto} = f F_\alpha(t)$, the first term in square brackets inside the integral simplifies, while the second term vanishes completely. F_α only appears in the boundary terms.

B. Constraint equations

The full set of Maxwell equations consists of the inhomogeneous equations Eq. (1.2) as well as the homogeneous constraints Eq. (1.3) which have to be satisfied by a solution to Eq. (1.2). In the usual approach introducing a vector potential A_α implies that the constraints are identically satisfied since they reduce to the Bianchi identities for the second derivatives of A_α. When solving for the components of the Faraday tensor directly there is no a priory guarantee that a solution to Eq. (2.15b) – (2.15f), and (2.3d) satisfies Eq. (1.3). It turns out, however, that a decomposition into spherical harmonics is sufficient to show that all but one of the constraints are identically satisfied. The one that is not identically true is the $tr\varphi$ (or $tr\theta$) equation, which in terms of ψ, χ and ξ reads

$$\frac{\psi}{r^2} - \frac{\chi_{,t}}{f} + \xi_{,r} = 0. \quad (2.18)$$

If the fields satisfy the sourced Maxwell equations Eqs. (2.3a), (2.3b), then Eq. (2.18) is just the evolution equation for ψ. Thus Eq. (2.18) is valid whenever ψ satisfies the consistency relations Eq. (2.13) and (2.14).

Analytically then, the situation is clear. Given a set of compatible initial conditions for ψ, χ and ξ which initially satisfy the constraint equations, a solution to the system of Eq. (2.15b) – (2.15f), (2.3d) satisfies the full set of Maxwell equations at all later times, too.

Numerically I monitor but do not enforce Eq. (2.13) and (2.14). I generally find that violations of the constraints are at least three orders of magnitude smaller than the field quantities themselves. Figures 1 and 2 compare χ obtained from its evolution equations to that obtained from Eq. (2.14).

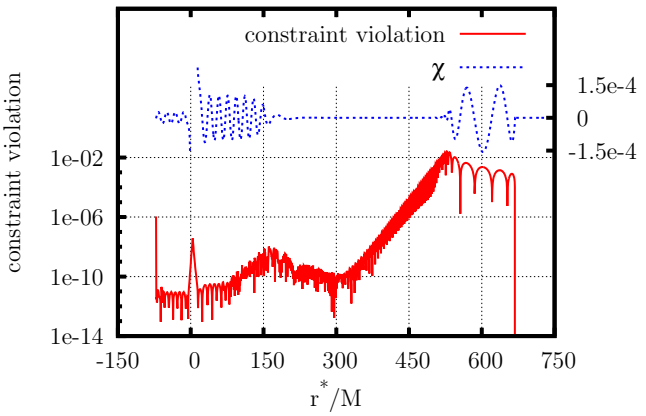

FIG. 1: Violations of the constraint $Z_\chi = \chi + \frac{1}{\ell(\ell+1)}\frac{\partial\psi}{\partial t} = 0$ in the vacuum region away from the location of particle. I plot the χ and $\log_{10}|Z_\chi|$ as obtained on a spatial slice at time $t = 600\,M$. For this slightly eccentric orbit ($p = 7.0$, $e = 0.3$) using a stepsize $h = 1/512M$ the errors in the $\ell = 2$, $m = 2$ mode are at least three orders of magnitude smaller than the field values. The exponentially growing signal between $300M \lesssim r^* \lesssim 500$ is a remnant of the initial data pulse travelling outward.

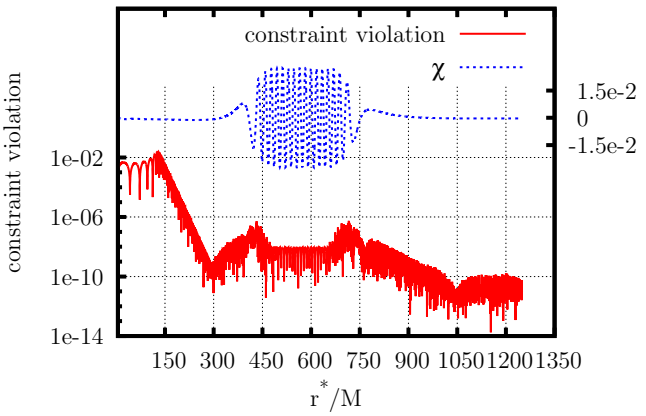

FIG. 2: Violations of the constraint $Z_\chi = \chi + \frac{1}{\ell(\ell+1)}\frac{\partial\psi}{\partial t} = 0$ at the location of the particle as a function of time. I display χ and $\log_{10}|Z_\chi|$ for the $\ell = 5$, $m = 3$ mode of a particle on an eccentric orbit with $p = 7.8001$, $e = 0.9$ with stepsize $h = 1/256\,M$. During the time $400\,M \lesssim t \lesssim 800\,M$ the particle is in the whirl phase. The exponentially decaying signal before $t \approx 250M$ is the initial data pulse.

C. Monopole mode

For the electromagnetic field, the monopole mode $\ell = 0$ is non-radiative. The vector harmonics $Z_A^{\ell m}$ and $X_A^{\ell m}$ cannot be defined in this case and the only surviving multipole mode is ψ. For the monopole case Eq. (2.15b)

reduces to a wave equation in flat space

$$\frac{\partial^2\psi}{\partial r^{*2}} - \frac{\partial^2\psi}{\partial t^2} = 4\pi f\left[\frac{\partial(r^2 j_t^{0,0})}{\partial r} - \frac{\partial(r^2 j_r^{0,0})}{\partial t}\right], \quad (2.19)$$

which is simple enough so that I can solve it analytically. A straightforward calculation shows that

$$\psi(t, r^*) = -\sqrt{4\pi} q\theta(r^* - r_0^*(t)) \quad (2.20)$$

satisfies Eq. (2.19) and corresponds to no outgoing radiation $(\partial_t - \partial_{r^*})\psi = 0$ at the event horizon and no ingoing radiation $(\partial_t + \partial_{r^*})\psi = 0$ at spatial infinity.

D. Discretization—even sector

Lousto's method is directly applicable to terms of the form $-\frac{\partial^2\psi}{\partial t^2} + \frac{\partial^2\psi}{\partial r^{*2}}$, $V(r)\psi$ (ie. the wave operator and potential terms) on the left-hand side of the equation and the source terms $S_\alpha(t)$ on the right hand side. Here ψ is used as a placeholder for any one of ψ, χ or ξ; $V(r)$ is an expression depending only on r. I discretize these as

$$\iint_{\text{cell}} \mathrm{d}u\,\mathrm{d}v\,\left(-\frac{\partial^2\psi}{\partial t^2} + \frac{\partial^2\psi}{\partial r^{*2}}\right) = -4\left[\psi_3 + \psi_2 - \psi_1 - \psi_4\right], \quad (2.21)$$

$$\iint_{\text{cell}} \mathrm{d}u\,\mathrm{d}v\,V(r)\psi = \begin{cases} h^2 V_0 \sum_i \psi_i + O(h^4) & \text{vacuum cells} \\ V_0 \sum_i A_i\psi_i + O(h^3) & \text{sourced cells,} \end{cases} \quad (2.22)$$

and

$$\iint_{\text{cell}} \mathrm{d}u\,\mathrm{d}v\,S_\alpha(t) = 2\int_{t_1}^{t_2} G_\alpha(t, r_0(t))\,\mathrm{d}t \pm \frac{2F_\alpha(t_1, r_0(t_1))}{1 - 2M/r(t_1)}[1 \mp \dot{r}_0(t_1)/E]^{-1} \pm \frac{2F_\alpha(t_2, r_0(t_2))}{1 - 2M/r(t_2)}[1 \pm \dot{r}_0(t_2)/E]^{-1}, \quad (2.23)$$

where $u = t - r^*$, $v = t + r^*$ are null coordinates, $\psi_1, \ldots, \psi_4$ refer to values of the field at the points labelled 1,...,4 in Fig. 3, $h = \Delta_t = \Delta_{r^*}/2$ is the step size, V_0 is the value of the potential at the centre of the cell, $A_1, \ldots, A_4$ are the areas indicated in Fig. 3 and t_1 and t_2 are the times at which the particle enters and leaves the cell, respectively.

Spelled out explicitly the evolution equations for vacuum cells are

$$\psi_3 = -\psi_2 + (1 - \frac{h^2}{2}V_0)(\psi_1 + \psi_4), \quad (2.24a)$$

$$\chi_3 = -\chi_2 + (1 - \frac{h^2}{2}V_0)(\chi_1 + \chi_4), \quad (2.24b)$$

$$\xi_3 = -\xi_2 + (1 - \frac{h^2}{2}V_0)(\xi_1 + \xi_4) - \frac{h^2}{4}V_{\xi,0}(\psi_1 + \psi_2 + \psi_3 + \psi_4), \quad (2.24c)$$

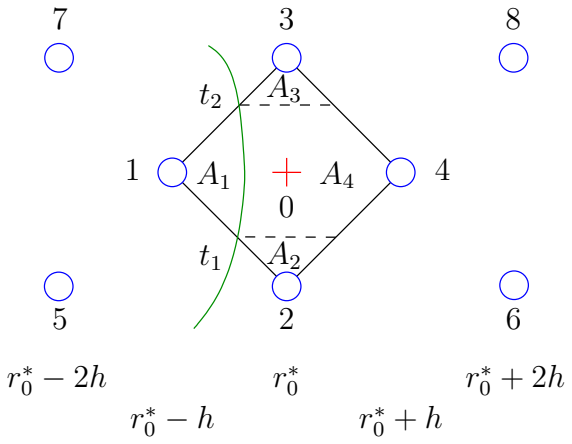

FIG. 3: Points used to calculate the integral over the potential terms. Grid points are indicated by blue circles.

and for sourced cells

$$\psi_3 = -[1 + \frac{V_0}{4}(A_2 - A_3)]\psi_2 + [1 - \frac{V_0}{4}(A_4 + A_3)]\psi_4 + [1 - \frac{V_0}{4}(A_1 + A_3)]\psi_1 - \frac{1}{4}(1 - \frac{V_0}{4}A_3)\iint \mathrm{d}u\,\mathrm{d}v\,S_\psi(t), \quad (2.25a)$$

$$\chi_3 = -[1 + \frac{V_0}{4}(A_2 - A_3)]\chi_2 + [1 - \frac{V_0}{4}(A_4 + A_3)]\chi_4 + [1 - \frac{V_0}{4}(A_1 + A_3)]\chi_1 - \frac{1}{4}(1 - \frac{V_0}{4}A_3)\iint \mathrm{d}u\,\mathrm{d}v\,S_\chi(t), \quad (2.25b)$$

$$\xi_3 = -[1 + \frac{V_0}{4}(A_2 - A_3)]\xi_2 + [1 - \frac{V_0}{4}(A_4 + A_3)]\xi_4 + [1 - \frac{V_0}{4}(A_1 + A_3)]\xi_1 - \frac{1}{4}V_{\xi,0}(A_1\psi_1 + A_2\psi_2 + A_3\psi_3 + A_4\psi_4) - \frac{1}{4}(1 - \frac{V_0}{4}A_3)\iint \mathrm{d}u\,\mathrm{d}v\,S_\xi(t). \quad (2.25c)$$

E. Discretization–odd sector

When written in terms of r^*, Eq. (2.3d), which governs the odd modes $\tilde{v}^{\ell m}$, is

$$\frac{\partial^2\tilde{v}_{\ell m}}{\partial r^{*2}} - \frac{\partial^2\tilde{v}_{\ell m}}{\partial t^2} - \frac{\ell(\ell+1)(r-2M)}{r^3}\tilde{v}_{\ell m} = -4\pi f j^{\text{odd}}_{\ell m}, \quad (2.26)$$

$$j^{\text{odd}}_{\ell m} = -\frac{qJ}{\ell(\ell+1)Er_0^2}\partial_\theta \bar{Y}^{\ell m}(\frac{\pi}{2}, \varphi_0)\delta(r^* - r_0^*). \quad (2.27)$$

Eq. (2.26) is of the form of the scalar wave equation discussed in paper II. I re-use the fourth order numerical code described there with $V = \frac{\ell(\ell+1)(r-2M)}{r^3}$, $S =$

$4\pi\frac{qfJ}{\ell(\ell+1)Er_0^2}\partial_\theta\bar{Y}^{\ell m}(\frac{\pi}{2},\varphi_0)$. This yields accurate results for $\tilde{v}$ and its derivatives.

III. INITIAL VALUES AND BOUNDARY CONDITIONS

I follow the approach detailed in paper II for the scalar self-force and do not specify physical initial data or an outer boundary condition. I arbitrarily choose the fields to vanish on the characteristic slices $u = u_0 = t_0 - r_0^*$ and $v = v_0 = t_0 + r_0^*$

$$\psi(u = u_0) = \psi(v = v_0) = 0, \tag{3.1}$$

thereby adding a certain amount of spurious waves to the solution which show up as an initial burst.

I implement ingoing wave boundary conditions near the event horizon, sufficiently close that *numerically* $r \approx 2M$, so that the potential terms in Eqs. (2.15b) – (2.15f) vanish. This happens at $r^* \approx -73\,M$ and I implement the ingoing waves condition $\partial_u\psi = 0$ there. Near the outer boundary this is not possible, since the potential decays slowly. Instead I choose to evolve the full domain of dependence of the initial data surface, hiding the effects of the boundary.

IV. PARTICLE MOTION

I use the same approach as described in paper II to evolve the particle's motion, i.e. I introduce the semi-latus rectum p, the eccentricity e and a fictitious angle χ, not to be confused with the Faraday tensor component χ defined in Eq. (2.8), such that

$$r(\tau) = \frac{pM}{1 + e\cos\chi(\tau)}. \tag{4.1}$$

The evolution is then governed by

$$\frac{\mathrm{d}\chi}{\mathrm{d}t} = \frac{(p-2-2e\cos\chi)(1+e\cos\chi)^2}{(Mp^2)} \times\sqrt{\frac{p-6-2e\cos\chi}{(p-2-2e)(p-2+2e)}}, \tag{4.2}$$

$$\frac{\mathrm{d}\varphi}{\mathrm{d}t} = \frac{(p-2-2e\cos\chi)(1+e\cos\chi)^2}{p^{3/2}M\sqrt{(p-2-2e)(p-2+2e)}}. \tag{4.3}$$

I use the embedded Runge-Kutta-Fehlberg (4, 5) algorithm provided by the GNU Scientific Library routine `gsl_odeiv_step_rkf45` and an adaptive step-size control to evolve the position of the particle forward in time.

V. EXTRACTION OF FIELD DATA AT THE PARTICLE

I use a straightforward one-sided extrapolation of field values to the right of the particle's position to extract values for ψ and $\partial_{r^*}\psi$. Specifically I fit a fourth order polynomial

$$p(x) = \sum_{n=0}^{4}\frac{c_i}{n!}x^n, \tag{5.1}$$

where $x = r^* - r_0^*$ to the five points to the right of the particle's current position and extract ψ and $\partial_{r^*}\psi$ as c_0 and c_1, respectively. In order to calculate $\frac{\partial\psi(t_0,r_0^*)}{\partial t}$ I follow [14] and calculate $\frac{\mathrm{d}\psi(t,r^*(t))}{\mathrm{d}t}$ on the world line of the particle. Since this can be calculated using either the field values on the world line

$$\frac{\mathrm{d}\psi\big(t,r^*(t)\big)}{\mathrm{d}t} = \frac{\psi\big(t+h,r^*(t+h)\big) - \psi\big(t-h,r^*(t-h)\big)}{2h} + O(h^2), \tag{5.2}$$

or as

$$\frac{\mathrm{d}\psi\big(t,r^*(t)\big)}{\mathrm{d}t} = \frac{\partial\psi}{\partial t} + \frac{\partial\psi}{\partial r^*}\frac{\mathrm{d}r_0^*}{\mathrm{d}t}, \tag{5.3}$$

where both $\frac{\partial\psi}{\partial r^*}$ and $\frac{\mathrm{d}r_0^*}{\mathrm{d}t} = \dot{r}_0/E$ are known, this allows me to find

$$\frac{\partial\psi}{\partial t} = \frac{\mathrm{d}\psi\big(t,r^*(t)\big)}{\mathrm{d}t} - \frac{\partial\psi}{\partial r^*}\frac{\mathrm{d}r_0^*}{\mathrm{d}t}. \tag{5.4}$$

I repeat this procedure to the left of the particle. As a check for the extraction procedure, I compare the difference between the right hand and left hand values $[\psi] = \psi_{\mathrm{right}} - \psi_{\mathrm{left}}$ with the analytically calculated jump conditions of appendix D 1. Similarly I check whether the numerical solutions obtained for χ and ξ directly are consistent with Eqs. (2.14) and (2.13), which give them in terms of derivatives of ψ.

VI. REGULARIZATION OF THE MODE SUM

The regularization procedure operates on scalar spherical harmonic modes of the multipole coefficients $F^{\ell m}_{(\mu)(\nu)}$ of the Faraday tensor. As a first step I use the auxiliary fields ψ, χ and ξ to reconstruct

$$A^{\ell' m'}_{r,t} - A^{\ell' m'}_{t,r} = \frac{\psi}{r^2}, \tag{6.1a}$$

$$\partial_t v^{\ell' m'} - A^{\ell' m'}_t = -\xi, \tag{6.1b}$$

and

$$\partial_r v^{\ell' m'} - A^{\ell' m'}_r = -\frac{\chi}{f}, \tag{6.1c}$$

the combinations of the vector potential modes needed to obtain the even sector of a tensor spherical harmonic decomposition of the Faraday tensor. The auxiliary field

$\tilde{v}$ and its derivatives provide the odd sector of the decomposition.

Using the comples pseudo-Cartesian tetrad $e^{\alpha}_{(0)}$, $e^{\alpha}_{(\pm)}$ and $e^{\alpha}_{(3)}$ introduced in paper I, I define tetrad components

$$F^{\rm ret}_{(\mu)(\nu)} \equiv F^{\rm ret}_{\alpha\beta} e^{\alpha}_{\ (\mu)} e^{\beta}_{\ (\nu)} \tag{6.2}$$

of the Faraday tensor.

I construct the spherical harmonic modes of $F^{\rm ret}_{(\mu)(\nu)}$ using the coupling coefficients displayed in Eq. (A4).

$$\begin{aligned} F^{\ell m,{\rm ret}}_{(\mu)(\nu)} = \sum_{\ell',m'} \Big[& C^{ab}_{(\mu)(\nu)}(\ell' m'|\ell m) \left(A^{\ell' m'}_{b,a} - A^{\ell' m'}_{a,b} \right) \\ & + D^{a}_{(\mu)(\nu)}(\ell' m'|\ell m) \left(\partial_a v^{\ell' m'} - A^{\ell' m'}_{a} \right) \\ & + E^{a}_{(\mu)(\nu)}(\ell' m'|\ell m) \partial_a \tilde{v}^{\ell' m'} \\ & + E_{(\mu)(\nu)}(\ell' m'|\ell m) \tilde{v}^{\ell' m'} \Big] \end{aligned}$$

I calculate the multipole coefficients of $F^{\ell,{\rm ret}}_{(\mu)(\nu)}$ as

$$F^{\ell,{\rm ret}}_{(\mu)(\nu)} = \sum_{m} F^{\ell m,{\rm ret}}_{(\mu)(\nu)}(t, r_0) Y_{\ell m}(\frac{\pi}{2}, \varphi_0), \tag{6.3}$$

and regularize them as in Eq. (1.5).

$$\begin{aligned} F^{R}_{(\mu)(\nu)} = \sum_{\ell} \Big\{ & F^{\ell,{\rm ret}}_{(\mu)(\nu)} - q \Big[A_{(\mu)(\nu)} \left(\ell + \frac{1}{2} \right) + B_{(\mu)(\nu)} + \\ & \frac{C_{(\mu)(\nu)}}{\ell + \frac{1}{2}} + \frac{D_{(\mu)(\nu)}}{(\ell - \frac{1}{2})(\ell + \frac{3}{2})} \Big] \Big\} \end{aligned} \tag{6.4}$$

I calculate the regularized self-force using $F^{R}_{(\mu)} = q F^{R}_{(\mu)(\nu)} u^{(\nu)}$. Finally I reconstruct the vector components of the self-force by from the tetrad components

$$F^{R}_{t} = \sqrt{f_0} F^{R}_{(0)}, \tag{6.5a}$$

$$F^{R}_{r} = \frac{1}{\sqrt{f_0}} {\rm Re} \left(F^{R}_{(+)} e^{-i\varphi_0} \right), \tag{6.5b}$$

$$F^{R}_{\phi} = r_0 \, {\rm Im} \left(F^{R}_{(+)} e^{-i\varphi_0} \right). \tag{6.5c}$$

VII. NUMERICAL TESTS

In this section I present the tests I performed to validate my numerical evolution code. I performed the same set of tests as described in paper II. First, in order to check the second-order convergence rate of the code, I performed regression runs with increasing resolution. As a second test, I computed the regularized self-force for several different combinations of orbital elements p and e and checked that the multipole coefficients decay with ℓ as expected. This provided a very sensitive check on the overall implementation of the numerical scheme as well as the analytical calculations that lead to the regularization parameters.

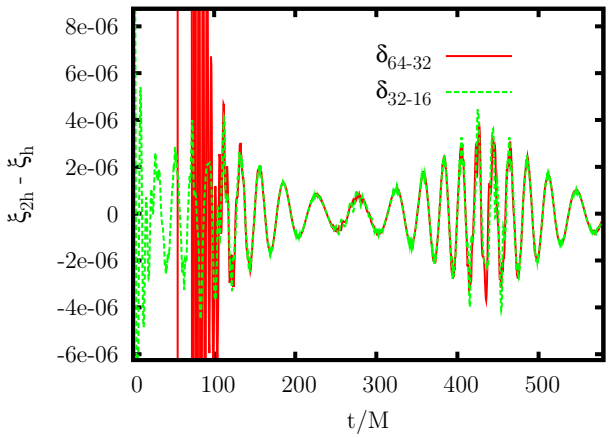

FIG. 4: Convergence test of the numerical algorithm in the sourced case. I show differences between simulations using different step sizes of 16, 32 and 64 cells per M. Displayed are the rescaled differences $\delta_{32-16} = \xi(h = 1/32M) - \xi(h = 1/16M)$ etc. of the field values at the position of the particle for a simulation with $\ell = 6$, $m = 4$ and $p = 7$, $e = 0.3$. I see that the convergence is approximately second-order. The curves are rescaled in such a way as to provide an estimate for the error of the highest resolution run compared to the real ($h \equiv 0$) solution.

A. Convergence tests

Convergence tests are a straightforward way to test the implementation of a numerical scheme. I performed regression runs for my second-order convergent code using a non-zero charge q and an eccentric orbit. I extract the field at the position of the particle, and thus also test the implementation of the extraction algorithm described in section V. I choose the $\ell = 6$, $m = 4$ mode of the field generated by a particle on a mildly eccentric geodesic orbit with $p = 7$, $e = 0.3$. As shown in Fig. 4 the convergence is approximately of second order. In the region $150\,M \lesssim t \lesssim 400\,M$ the two curves lie on top of each other, as expected for a second-order convergent algorithm. In the region from $400\,M$ to $450\,M$ there is some difference between the two lines, caused by cell crossing effects similar to those discussed in paper II.

B. Discontinuity across the world line

The singular source term on the right hand side of Eqs. (2.15b) – (2.15f) implies that the fields ψ, χ and ξ are discontinuous across the world line. Since the jump conditions can be calculated analytically as done in appendix D 1, I can check whether the numerical results faithfully reproduce the expected behaviour. Using the methods described in section V I obtain one-sided extrapolation for the field values and their spatial derivatives. For the highest resolution run used in the regression analysis in section VII A I find that the numerical results for

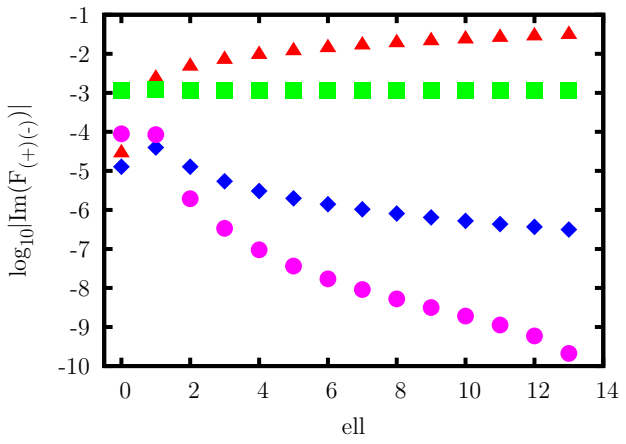

FIG. 5: Multipole coefficients of the dimensionless Faraday tensor component $\frac{M^2}{q}\,\mathrm{Im}\,F^R_{(+)(-)}$ for a particle on an eccentric orbit ($p = 7.2$, $e = 0.5$). The coefficients are extracted at $t = 500\,M$ along the trajectory shown in Fig. 6. The plots show several stages of the regularization procedure, with a closer description of the curves to be found in the text. A uniform stepsize of $h = 1/512\,M$ was used.

ξ agree with the analytical calculation of the jump condition up to terms of the order of 10^{-8}; two orders of magnitude smaller than the estimated numerical error of 10^{-6}. For $\partial_{r^*}\xi$ the situation is reversed, with the numerical error in the jump condition being about an order of magnitude larger than the numerical error in the field derivative itself. The accuracy of the numerical derivatives is therefore limited by the accuracy of the extraction scheme, resulting in about three significant figures for the set of parameters displayed in Fig. 4. However the regularization calculation is constructed in such a way that no derivatives of the fields need be obtained in order to calculate the self-force. I therefore feel that I can accept the reduced accuracy provided by the simple extraction scheme.

C. High-ℓ behaviour of the multipole coefficients

Inspection of Eq. (1.5) reveals that a plot of $F^\ell_{(\mu)(\nu)}$ as a function of ℓ (for a fixed value of t) should display a linear growth in ℓ for large ℓ. Removing the $A_{(\mu)(\nu)}$ term should produce a constant curve, removing the $B_{(\mu)(\nu)}$ term (given that $C_{(\mu)(\nu)} = 0$) should produce a curve that decays as ℓ^{-2}, and finally, removing the $D_{(\mu)(\nu)}$ term should produce a curve that decays as ℓ^{-4}. It is a powerful test of the overall implementation to check whether the numerical data behaves as expected. Fig. 5 plots the remainders as obtained from my numerical simulation, demonstrating the expected behaviour. It displays, on a logarithmic scale, the absolute value of $\mathrm{Im}\,F^{\ell,R}_{(+)(-)}$, the imaginary part of the $F^R_{(+)(-)}$ tetrad component of the Faraday tensor. The orbit is eccentric ($p = 7.2$, $e = 0.5$), and all components of the self-force require regularization. The first curve (in triangles) shows the unregularized multipole coefficients that increase linearly in ℓ, as confirmed by fitting a straight line to the data. The second curve (in squares) shows partially regularized coefficients, obtained after the removal of $(\ell+1/2)A_{(\mu)(\nu)}$; this clearly approaches a constant for large values of ℓ. The curve made up of diamonds shows the behaviour after removal of $B_{(\mu)(\nu)}$; because $C_{(\mu)(\nu)} = 0$, it decays as ℓ^{-2}, a behaviour that is confirmed by a fit to the $\ell \geq 5$ part of the curve. Finally, after removal of $D_{(\mu)(\nu)}/[(\ell-\frac{1}{2})\,(\ell+\frac{3}{2})]$ the terms of the sum decrease in magnitude approximately as ℓ^{-4} when fitting to the data points $\ell \geq 7$. This result depends slightly on the range of points used for the fit. I expect this to be due to the fact that I stop at $\ell = 15$, which seems to be not large enough to show the asymptotic behaviour. Extending the range to very high values of ℓ proved to be very difficult, since the numerical code is only second order convergent, so that the numerical errors become dominant by the time the asymptotic behaviour begins to show.

Each one of the last two curves would result in a converging sum, but the convergence is faster after subtracting the $D_{(\mu)(\nu)}$ terms. I thereby gain about one order of magnitude in the accuracy of the estimated sum.

Figure 5 provides a sensitive test of the implementation of both the numerical and analytical parts of the calculation. Small mistakes in either one will cause the difference in Eq. (1.5) to have a vastly different behaviour.

D. Accuracy of the numerical method

In this work I are less demanding with the numerical accuracy then I were in paper II, where I describe a very high accuracy numerical code. Implementing suach a code is very tedious even for the scalar case, and much more so for the electromagnetic case treated here. Therefore I implement a simpler method that allows me to access the physics of the problem without being hindered by technical problems due to a complicated numerical method.

An estimate for the truncation error arising from cutting short the summation in Eq. (1.5) at some $\ell_{\max}$ can be calculated by considering the behaviour of the remaining terms for large ℓ. Detweiler et. al. [15] showed that the remaining terms scale as ℓ^{-4} for large ℓ. They find the functional form of the terms to be

$$\frac{E\mathcal{P}_{3/2}}{(2\ell-3)(2\ell-1)(2\ell+3)(2\ell+5)}, \tag{7.1}$$

where $\mathcal{P}_{3/2} = 36\sqrt{2}$. I fit a function of this form to the tail end of a plot of the multipole coefficients to find the coefficient E in Eq. (7.1). Extrapolating to $\ell \to \infty$ I find

error estimation	mildly eccentric orbit
relative truncation error in $\frac{M^2}{q^2}\,\mathrm{Re}(F^R_{(+)})$	2×10^{-4}
relative discretization error in $\frac{M^2}{q}\psi$	$\approx 10^{-7}$

TABLE I: Estimated values for the various errors in the components of the self-force as described in the text. I show the truncation and discretization errors for the mildly eccentric orbit ($p = 7.2$, $e = 0.5$). The truncation error is calculated using a plot similar to the one shown in Fig. 5. The discretization error is estimated using a plot similar to that in Fig. 4 for the $\ell = 2$, $m = 2$ mode.

that the truncation error is

$$\varepsilon = \sum_{\ell=\ell_{\max}}^{\infty} [\text{Eq. (7.1)}] \tag{7.2}$$

$$= \frac{12\sqrt{2}E\ell_{\max}}{(2\ell_{\max}+3)(2\ell_{\max}+1)(2\ell_{\max}-1)(2\ell_{\max}-3)}, \tag{7.3}$$

where $\ell_{\max}$ is the value at which I cut the summation short.

A second source of error lies in the numerical calculation of the retarded solution to the wave equation. This error depends on the step size h used to evolve the field forward in time. For a numerical scheme of a given convergence order, I can estimate this discretization error by extrapolating from simulations using different step sizes down to $h = 0$. This is what was done in the graphs shown in Sec. VII A.

I display results for the mildly eccentric orbit shown in Fig. 6 with data extracted at $t = 500\,M$, that is at the instant shown in Fig. 5. At this moment, the multipole coefficients of $\mathrm{Re}(F^R_{(+)})$ decay as expected, but e.g. the $\mathrm{Im}(F^R_{(+)})$ component decays faster with ℓ for the range of modes $0 \le \ell \le 13$ modes that were calculated. I choose an orbit of low eccentricity as high eccentricity causes the field values to be plagued by high frequency noise, as discussed in paper II. This makes it impossible to reliably estimate the discretization error for these orbits.

Table I lists typical values for the errors discussed above.

VIII. SAMPLE RESULTS

In this section I describe some results obtained from my numerical calculation.

A. Mildly eccentric orbit

I choose a particle on an eccentric orbit with $p = 7.2$, $e = 0.5$ which starts at $r = pM/(1-e^2)$, halfway between periastron and apastron. The field is evolved for $600\,M$ with a uniform resolution of 512 grid points per M, both in the t and r^* directions, for all values of ℓ. Multipole coefficients for $1 \le \ell \le 15$ are calculated and used to reconstruct the regularized self-force F_α along the geodesic. Figure 7 shows the result of the calculation. For the choice of parameters used to calculate the force shown in Fig. 7, the error bars corresponding to the truncation error Eq. (7.2) (which are already much larger than than the discretization error) would be of the order of the line thickness and have not been drawn.

Already for this small eccentricity, I see that the self-force is most important when the particle is closest to the black hole (ie. for $200\,M \lesssim t \lesssim 400\,M$). The self-force acting on the particle is very small once the particle has moved away to $r \approx 15\,M$.

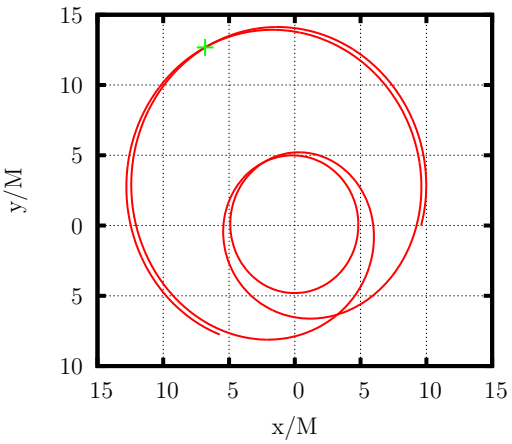

FIG. 6: Trajectory of a particle with $p = 7.2$, $e = 0.5$. The cross-hair indicates the point where the data for Fig. 5 was extracted.

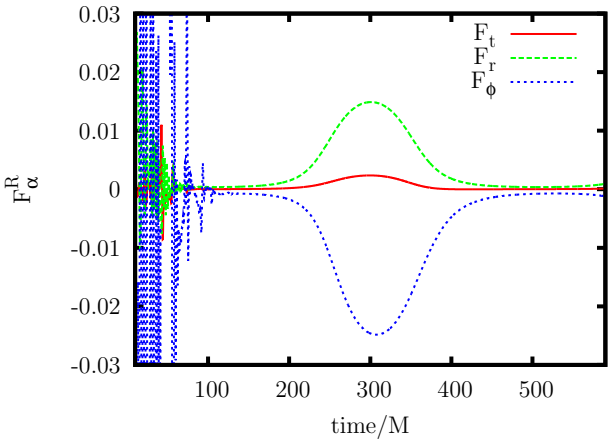

FIG. 7: Regularized dimensionless self-force $\frac{M^2}{q^2}F_t$, $\frac{M^2}{q^2}F_r$ and $\frac{M}{q^2}F_\phi$ on a particle on an eccentric orbit with $p = 7.2$, $e = 0.5$.

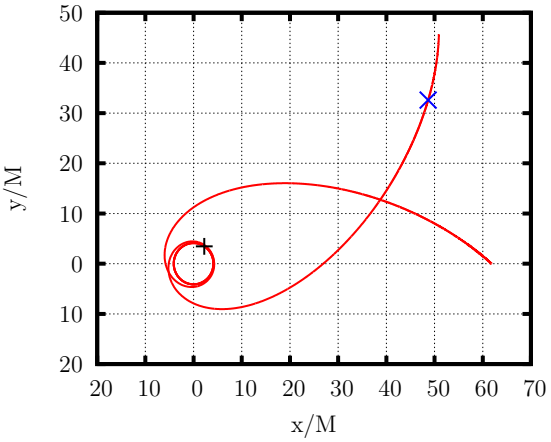

FIG. 8: Trajectory of a particle on a zoom-whirl orbit with $p = 7.8001$, $e = 0.9$. The cross-hairs indicate the positions where the data shown in Fig. 10 and 11 was extracted.

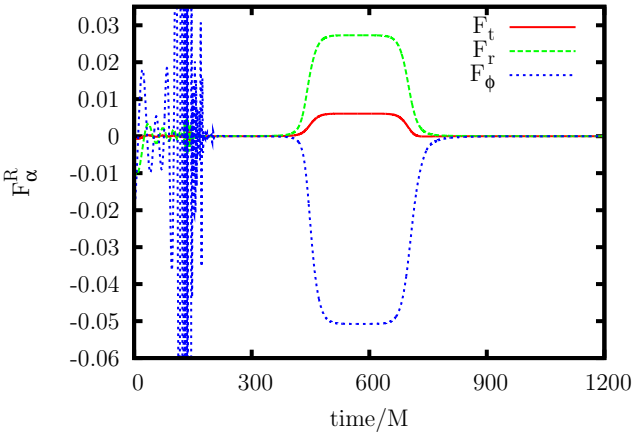

FIG. 9: Self-force acting on a particle. Shown is the dimensionless self-force $\frac{M^2}{q^2}F_t$, $\frac{M^2}{q^2}F_r$ and $\frac{M}{q^2}F_\phi$ on a zoom-whirl orbit with $p = 7.8001$, $e = 0.9$. No error bars showing an estimate error are shown, as the errors shown are to small to show up on the graph. Notice that the self-force is essentially zero during the zoom phase $900\,M \lesssim t \lesssim 1200\,M$ and reaches a constant value very quickly after the particle enters into the whirl phase.

B. Zoom-whirl orbit

Particles on highly eccentric orbits are of most interest as sources of gravitational radiation. For nearly parabolic orbits with $e \lesssim 1$ and $p \gtrsim 6 + 2e$, a particle revolves around the black hole a number of times, moving on a nearly circular trajectory close to the event horizon ("whirl phase"), before moving away from the black hole ("zoom phase"). During the whirl phase the particle is in the strong field region of the spacetime, emitting copious amounts of radiation. Figures 8 and 9 show the trajectory of a particle and the force on such an orbit with $p = 7.8001$, $e = 0.9$ calculated using a uniform step size of $h = 1/256$ throughout the range $1 \le \ell \le 15$. Even more so than for the mildly eccentric orbit discussed in Sec. VIII A, the self-force (and thus the amount of radiation produced) is much larger while the particle is close to the black hole than when it zooms out. The force graph is very similar to that obtained for the scalar self-force in paper II, however the overshooting behaviour at the onset and near the end of the whirl phase is not as pronounced.

Since the rates of change in energy E and angular momentum J of the trajectory are directly related to the self-force

$$\dot{E} = -a_t, \qquad \dot{J} = a_\phi, \tag{8.1}$$

it is easy to see that the self-force shown in Fig. 9 confirms the expectation that the self-force decreases both the energy and angular momentum of the particle while radiation is emitted.

In Fig. 10 and Fig. 11 I show plots of $F^\ell_{(0)}$ constructed from $F^\ell_{(\mu)(\nu)}$ after the removal of the $A_{(\mu)(\nu)}$, $B_{(\mu)(\nu)}$, and $D_{(\mu)(\nu)}$ terms.

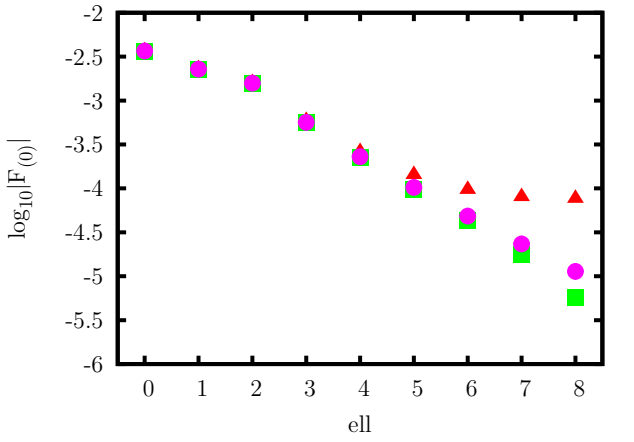

FIG. 10: Multipole coefficients of $\frac{M^2}{q}\,\mathrm{Re}\,F^R_{(0)}$ for a particle on a zoom-whirl orbit ($p = 7.8001$, $e = 0.9$). The coefficients are extracted at $t = 525\,M$ when the particle is deep within the whirl phase. Here $\dot{r} \approx 0$ and the behaviour of $F^R_{(\mu),\ell}$ is very close to that for a circular orbit, requiring very little regularization. Red triangles are used for the unregularized multipole coefficients $F_{(0),\ell}$, squares, diamonds and disks are used for the partly regularized coefficients after the removal of the $A_{(0)}$, $B_{(0)}$ and $D_{(0)}$ terms respectively.

IX. EFFECTS OF THE CONSERVATIVE SELF-FORCE

In this section only, I will use the subscript "0" to denote quantities evaluated on the unperturbed geodesic, and no subscript to denote quantities evaluated on the perturbed world-line.

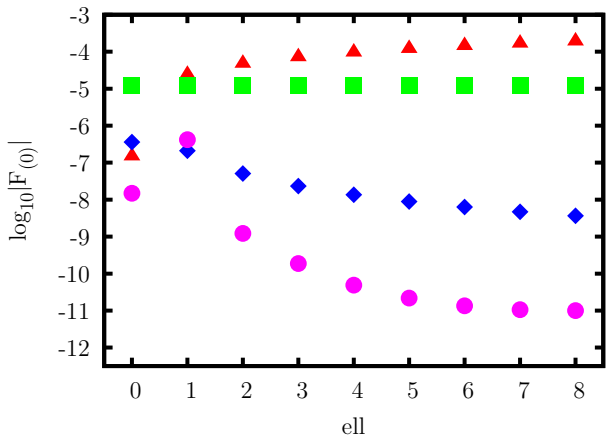

FIG. 11: Multipole coefficients of $\frac{M^2}{q}\,\mathrm{Re}\,F^R_{(0)}$ for a particle on a zoom-whirl orbit ($p = 7.8001$, $e = 0.9$). The coefficients are extracted at $t = 1100\,M$ when the particle is far away from the black hole. As $\dot{r}$ is non-zero, all components of the self-force require regularization and I see that the dependence of the multipole coefficients on ℓ is as predicted by Eq. 1.5. After the removal of the regularization parameters $A_{(\mu)(\nu)}$, $B_{(\mu)(\nu)}$, and $D_{(\mu)(\nu)}$ the remainder is proportional to ℓ^0, ℓ^{-2} and ℓ^{-4} respectively.

I follow the literature (see e.g. [6]) and define the dissipative part to be the half retarded minus half advanced force and the conservative part to be the half retarded plus half advanced force

$$F^{\rm diss}_\alpha \equiv \frac{1}{2}\left(F^{\rm ret}_\alpha - F^{\rm adv}_\alpha\right), \tag{9.1}$$

$$F^{\rm cons}_\alpha \equiv \frac{1}{2}\left(F^{\rm ret}_\alpha + F^{\rm adv}_\alpha\right). \tag{9.2}$$

The conservative force is the time reversal invariant part of the self-force. It does not affect the radiated energy or angular momentum fluxes $\dot{E}$ and $\dot{J}$; it shifts the values of E and J away from their geodesic values, affecting the orbital motion and the phase of the emitted waves.

To obtain expressions for E and J under the influence of the self-force, I employ the procedure described in [16]. I begin by writing down the normalization condition for the four velocity

$$-1 = u^\alpha u_\alpha = -\frac{E^2}{f} + \frac{J^2}{r^2}, \tag{9.3}$$

as well as the r-component of the geodesic equation

$$\frac{F^r}{m} = \ddot{r} - \frac{M}{(r-2M)r}\dot{r}^2 - \frac{(r-2M)J^2}{r^4} + \frac{ME^2}{(r-2M)r}, \tag{9.4}$$

where $F^r = qF^r{}_\mu u^\mu$ is the radial component of the self-force. Solving Eq. (9.3) and (9.4) I find

$$E^2 = E_0^2 - \frac{(r-2M)r}{r-3M}\frac{F^r}{m}, \tag{9.5}$$

$$J^2 = J_0^2 - \frac{r^4}{r-3M}\frac{F^r}{m}, \tag{9.6}$$

where

$$E_0^2 = \dot{r}^2 + \frac{(r-2M)r\ddot{r}}{r-3M} + \frac{(r-2M)^2}{(r-3M)r}, \tag{9.7}$$

$$J_0^2 = \frac{r^4\ddot{r}}{r-3M} + \frac{Mr^2}{r-3M}. \tag{9.8}$$

I stress that E_0 and J_0 are not the geodesic *values* for energy and angular momentum. They are of the correct form but are evaluated using the *accelerated* values for r, $\dot{r}$ and $\ddot{r}$ (instead of the geodesic values r_0, $\dot{r}_0$, etc.).

For small perturbing force of order ε I expand Eqs. (9.5) and (9.6) in terms of the perturbation strength and find

$$E = E_0 + \Delta E \approx E_0 - \varepsilon\frac{(r-2M)r}{2(r-3M)E_0}\frac{F^r}{m} + O(\varepsilon^2), \tag{9.9}$$

$$J = J_0 + \Delta J \approx J_0 - \varepsilon\frac{r^4}{2(r-3M)J_0}\frac{F^r}{m} + O(\varepsilon^2), \tag{9.10}$$

where F^r is evaluated with the help of the unperturbed four velocity $u^\alpha_0 = [E_0/f, \dot{r}_0, 0, J_0/r_0^2]$. The fractional changes $\Delta E/E_0$ and $\Delta J/J_0$ are given by

$$\Delta E/E_0 = -\varepsilon\frac{(r-2M)r}{2(r-3M)E_0^2}\frac{F^r}{m} + O(\varepsilon^2), \tag{9.11}$$

$$\Delta J/J_0 = -\varepsilon\frac{r^4}{2(r-3M)J_0^2}\frac{F^r}{m} + O(\varepsilon^2). \tag{9.12}$$

Once the perturbations in E and J are known, I calculate the change in the angular frequency

$$\Omega \equiv \frac{{\rm d}\varphi}{{\rm d}t} = \frac{r-2M}{r^3}\frac{J}{E}. \tag{9.13}$$

For small perturbing force I expand in powers of the perturbation strength

$$\Omega = \frac{r_0-2M}{r_0^3}\frac{J_0}{E_0}\left[1 - \varepsilon\left(\frac{r^4}{2(r-3M)J_0^2} - \frac{(r-2M)r}{2(r-3M)E_0^2}\right)\frac{F^r}{m}\right] + O(\varepsilon^2). \tag{9.14}$$

The relative change $\Delta\Omega/\Omega_0$ is given by

$$\Delta\Omega/\Omega_0 = -\varepsilon\left(\frac{r^4}{2(r-3M)J_0^2} - \frac{(r-2M)r}{2(r-3M)E_0^2}\right)\frac{F^r}{m} + O(\varepsilon^2). \tag{9.15}$$

A. Circular orbits

The effect of the conservative self-force is most clearly observed for circular orbits, where the unperturbed angular frequency Ω as well as the shift due to the perturbation are constant in time.

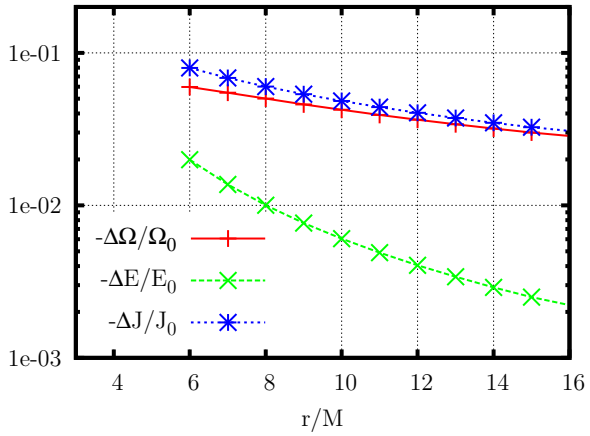

FIG. 12: Fractional change $\Delta\Omega/\Omega_0$ induced by the presence of the conservative self-force. The effect of the self-force is to move the radius of the orbit outward, decreasing its angular frequency.

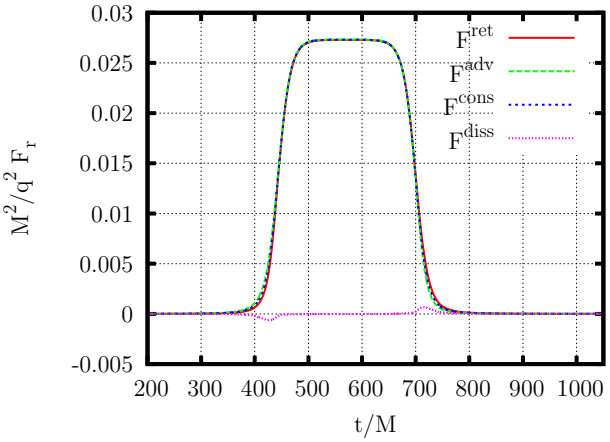

FIG. 13: r component of the dimensionless self-force acting on a particle on a zoom-whirl orbit ($p = 7.8001$, $e = 0.9$) around a Schwarzschild black hole. Shown are the retarded (solid, red), advanced (dashed, green), conservative (dotted, blue) and dissipative (finely dotted, pink) force acting on the particle.

For a particle in circular motion the self-force is constant in time and it turns out that the radial component is entirely conservative whereas the t and ϕ components are entirely dissipative. For circular orbits, the unperturbed values of E and J are given by

$$E_0 = \frac{r_0 - 2M}{\sqrt{r_0(r_0 - 3M)}}, \tag{9.16}$$

$$J_0 = r_0\sqrt{\frac{M}{r_0 - 3M}}, \tag{9.17}$$

and substituting these into Eq. (9.14) I find

$$\Omega = \sqrt{\frac{M}{r_0^3}} - \frac{(r_0 - 3M)}{2mM}\sqrt{\frac{M}{r_0}}F_r + O(\varepsilon^2), \tag{9.18}$$

where the first term is just the angular frequency for an unperturbed geodesic at radius r_0. The fractional change $\Delta\Omega/\Omega_0$ is then

$$\frac{\Delta\Omega}{\Omega_0} = -\frac{(r_0 - 3M)r_0}{2mM}F_r + O(\varepsilon^2). \tag{9.19}$$

Similarly the fractional changes in E and J: $\Delta E/E_0$ and $\Delta J/J_0$ are given by

$$\Delta E/E_0 = -\frac{r_0}{2m}F_r, \tag{9.20}$$

$$\Delta J/J_0 = -\frac{(r_0 - 2M)r_0}{2mM}F_r. \tag{9.21}$$

Figure 12 shows the fractional change in Ω_0, E and J as a function of the orbit's radius r_0.

B. Eccentric orbits

For eccentric orbits the self-force is no longer constant in time and I have to numerically calculate both the retarded and the advanced self-force in order to construct the conservative self-force. I find the advanced force by running the simulation backwards in time. That is I start the evolution on the very last time slice and evolve backwards in time until I reach the slice corresponding to $t = 0$. I reverse the boundary condition at the event horizon to be be outgoing radiation only $(\partial_t + \partial_{r^*})\psi = 0$ and adjust the outer boundary so as to simulate only the backwards domain of dependence of the initial slice. I do not change the trajectory of the particle. I do not change the regularization parameters, since they depend only on the local behaviour of the field and are insensitive to the boundary conditions far away.

1. *Conservative force on zoom-whirl orbits*

I calculate the conservative self-force on a zoom-whirl orbit with $p = 7.8001$, $e = 0.9$. Figs. 13 and 14 display the breakdown of the self-force into retarded and advanced, and conservative and dissipative parts for a particle on a zoom-whirl orbit. In both plots the force is very weak when the particle is in the zoom phase $t \lesssim 400\,M$ or $t \gtrsim 800\,M$ and nearly constant while the particle is in the whirl phase $400\,M \lesssim t \lesssim 800\,M$. Inspection of the behaviour of the r component reveals that it is almost exclusively conservative, with only a tiny dissipative effect when the particle enters or leaves the whirl phase. This result is consistent with the observation that the particle moves on a nearly circular trajectory while in the whirl phase, for which the radial component is precisely conservative. Similarly the ϕ component is almost entirely dissipative, with only a small conservative contribution when the particle enters or leaves the whirl phase, its maximum coinciding with that of $\ddot{r}$ (not shown on the graph).

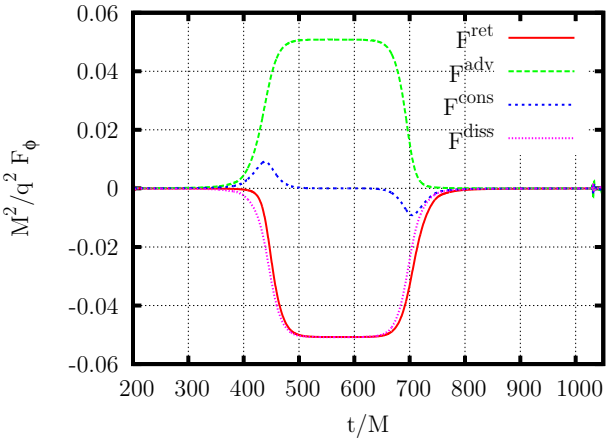

FIG. 14: φ component of the dimensionless self-force acting on a particle on a zoom-whirl orbit ($p = 7.8001$, $e = 0.9$) around a Schwarzschild black hole. Shown are the retarded (solid, red), advanced (dashed, green), conservative (dotted, blue) and dissipative (finely dotted, pink) force acting on the particle.

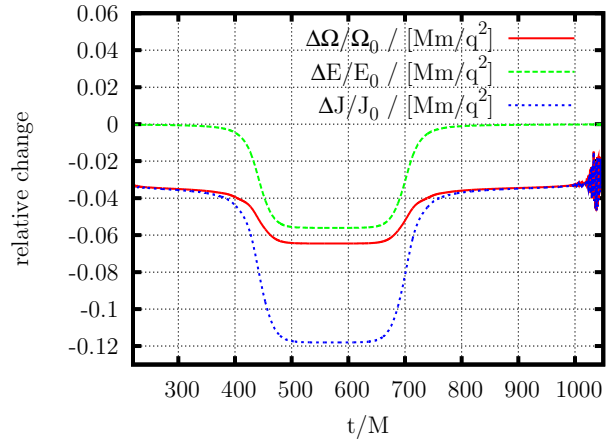

FIG. 15: Relative change in Ω, E, J for a particle on a zoom-whirl orbit due to the conservative electromagnetic self-force.

I calculate the relative changes in E, J and Ω under the influence of the self-force using Eqs. (9.11), (9.12), (9.15). Fig. 15 displays the relative changes $\Delta E/E_0$, $\Delta J/J_0$ and $\Delta\Omega/\Omega_0$ for a particle on a zoom whirl orbit $p = 7.8001$, $e = 0.9$. The change in E, J and Ω is strongest in the whirl phase when $r \approx 4.1M$. It is consistent with the shift experienced by a particle on a circular orbit at $4.1M$.

C. Effects on the innermost stable orbit

In the gravitational case, considerable work has been done to identify gauge invariant effects of the self-force [17, 18]. The electromagnetic self-force is not subject to the same ambiguity thus it can help shed light on the gravitational case as well by providing a clear distinction between kinetic and dynamic effects. In this section I calculate the effect of the conservative self-foce on the location of the innermost stable circular orbit around a Schwarzschild black hole. Such a calculation was first performed for the scalar self-force by [16], where a highly accurate frequency domain numerical scheme was used. Recently [7, 19] have extended this calculation to gravity, using their time domain code to perform the intergration of the wave equation. Since the code presented in this paper is in the time domain as well, it is closest in spirit to [19].

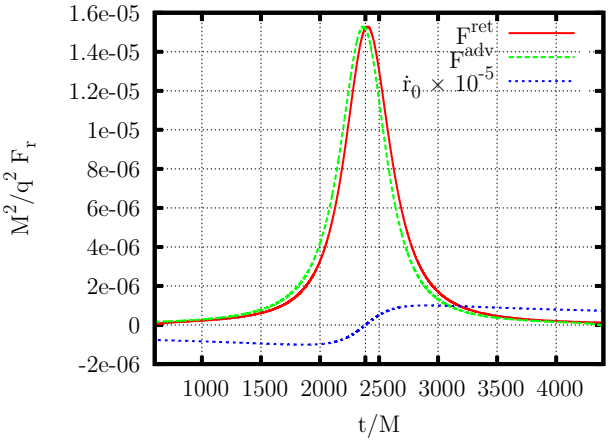

FIG. 16: r component of the dimensionless self-force acting on a particle on an orbit with $p = 78$, $e = 0.9$. Shown are the retarded and advanced forces as well as $\dot{r}$. The vertical line at $t \approx 2383\,M$ marks the time of closest approach to the black hole.

X. RETARDATION OF THE SELF-FORCE

For scalar perturbation in a weak gravitational field Poisson [20] showed that the self-force is delayed with respect to the particle motion by the light travel time from the particle to the central body and back to the particle again. In a spacetime where the central body is compact the treatment of [20] is no longer directly applicable, but I still expect some retardation in the self-force when compared to the particle's motion. To study this effect, I calculate the self-force on an eccentric orbit with $p = 78$, $e = 0.9$; ten times larger than the zoom-whirl orbit discussed earlier. The large orbit was chosen so as to be able to clearly see any possible retardation which might not be visible if the particle's orbit is deep within the strong field region close to the black hole. Figures 16 and 17 display plots of the r and ϕ components of the self-force acting on the particle close to periastron. Shown are the retarded and advanced forces as well as the particle's radial velocity $\dot{r}$. Without considering retardation I expect the self-force to be strongest when the particle is closest to the black hole, when $\dot{r} = 0$, as evident in Fig. 13. Clearly for the r component displayed in Fig. 16 the re-

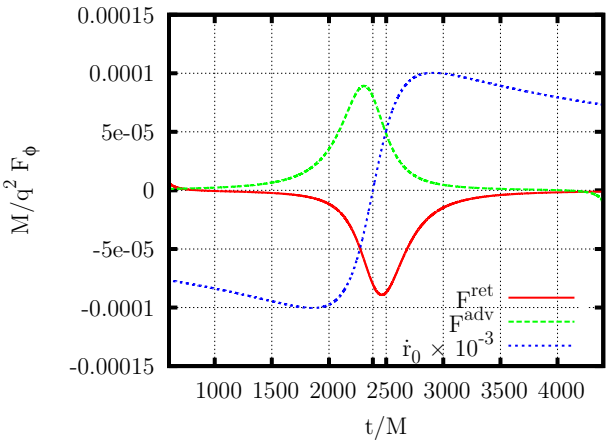

FIG. 17: ϕ component of the dimensionless self-force acting on a particle on an orbit with $p = 78$, $e = 0.9$. Shown are the retarded and advanced forces as well as $\dot{r}$. The vertical line at $t \approx 2383\,M$ marks the time of closest approach to the black hole.

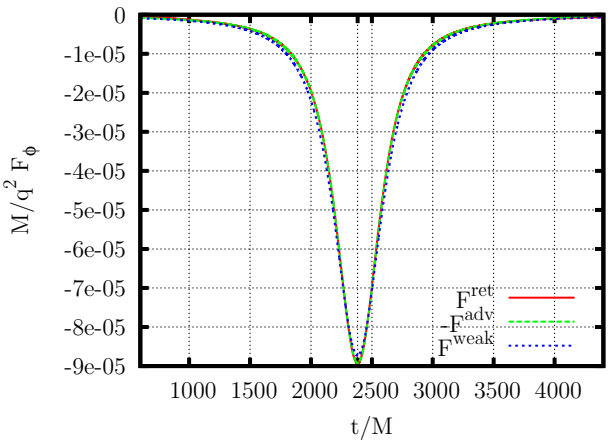

FIG. 18: ϕ component of the retarded (solid red line) and (dashed green line) negative advanced self-forces acting on a particle with $p = 78$, $e = 0.9$. The forces have been shifted by $\Delta t \approx 2[r_0(t) - 3.0\,M]$. Also shown is the self-force calculated using the weak field expression Eq. 11.1 (blue dotted line).

tarded and advanced forces both peak at a time very close to the zero crossing of $\dot{r}$, suggesting very little time delay in the r component of the self-force. In Fig. 17 on the other hand the retarded and advanced ϕ-component of the self-force peaks away from the time of closest approach $t_{\rm min}$. Inspection of the graph shows that the delay (advance) between the time of closest approach and the peak in the retarded (advanced) force is compatible with a delay of $\Delta t_{\rm min} \approx 2(r_{\rm min} - 3.0\,M) \approx 74\,M$. Using a delay of $\Delta t \approx 2[r_0(t) - 3.0\,M]$ and plotting $F^{\rm ret}_{\varphi}(t + \Delta t)$ and $-F^{\rm adv}_{\varphi}(t - \Delta t)$ versus t both curves visually lie on top of each other and the maximum is located at $t_{\rm min}$ as shown in Fig. 18 below. This suggests that the self-force is in large parts due to radiation that travels into the strong field region close to the black hole and is scattered back to the particle. The time delay can then be loosely interpreted as the time it takes the signal to travel to the light ring around the black hole and back to the particle. This interpretation is loose for two reasons: First r^* and not r is associated with the light travel time. Using r^*, however, does not lead to a better overlap of the curves once a suitable constant offset chosen. Second, for the zoom-whirl orbit shown in Fig. 9 the (shallow) maximum in the self-force is offset by only $\Delta t \approx 2[r_0(t) - 1.0\,M]$ which leads to a reasonable overlap of the two curves. Interestingly using r^* instead of r yields a worse overlap. For very large orbits $p = 780$, $e = 0.9$ it is impossible to read off the small constant offset to the dominant $2r_0(t)$ contribution.

XI. WEAK FIELD LIMIT

As a last application I use my code to compare the numerical self-force in the weak field region to the self-force calculated using the weak field expression

$$\boldsymbol{f}_{\rm self} = \lambda_c \frac{q^2}{m}\frac{M}{r^3}\hat{\boldsymbol{r}} + \lambda_{rr}\frac{2}{3}\frac{q^2}{m}\frac{{\rm d}\boldsymbol{g}}{{\rm d}t}, \qquad \boldsymbol{g} = -\frac{M}{r^2}\hat{\boldsymbol{r}}, \quad (11.1)$$

of [6, 21]. I calculate the self-force for a particle on an eccentric orbits with $e = 0.9$ and $p = 78$ or $p = 780$. Fig. 18 shows the retarded and (negative) advanced forces shifted by $\Delta t \approx 2[r_0(t) - 3.0\,M]$ as well as the analytic force calculated using Eq. (11.1). At this distance there are still some differences between the (shifted) retarded field and the weak field expression. One reason for this lies in the choice of a suitable r coordinate to correspond to the r coordinate in the weak field expression. In this work I use the areal Schwarzschild r, but the isotropic coordinate $\bar{r} = \frac{r-M}{2} + \frac{\sqrt{r\,(r-2*M)}}{2}$ or even the tortoise r^* could be used as well. Neither one yields a good agreement between the two curves.

For $p = 780$ using a shift of $\Delta t = 2r_0(t)$ the agreement between numerical data and analytic expression is excellent as is evident in Fig. 19. At this distance r, $\bar{r}$ and r^* are indistinguishable.

XII. CONCLUSIONS

I calculated the self-force acting a on an electromagnetic point charge in orbit around a Schwarzschild black hole. To do so I calculated the regularization parameters A,B, and D in section B and implemented a second order accurate numerical scheme in section II.

I find the behaviour of the electromagnetic self-force to be similar but not identical to that of the scalar self-force. In both cases the self-force is strongest when the particle is closest to the black hole. Further, during the whirl phase of a zoom-whirl orbit with its nearly constant

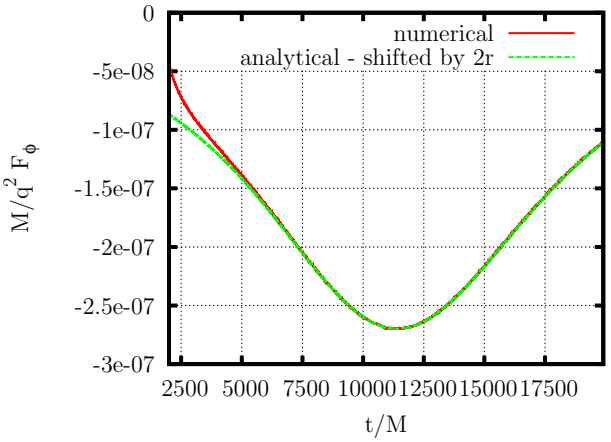

FIG. 19: ϕ component of the retarded self-force acting on a particle on an orbit with $p = 780$, $e = 0.9$ close to periastron. Shown are the numerical (solid, red) and shifted analytical (dashed, green) forces. The agreement between numerical and analytical calculation is excellent, the discrepancy for $t \lesssim 7500\,M$ is due to initial data contamination.

radius, the self-force is very close to that of a particle in circular orbit at this radius. On the other hand, the overshooting effect upon entering the whirl phase which was observed in the scalar case is much weaker in the electromagnetic case.

I calculated the effects of the conservative self-force on circular orbits, where it reduces the angular frequency and thus affects the phasing of the observed waves. I find this effect to be much stronger in the electromagnetic case than in the scalar case discussed in [16]. In particular during the nearly circular whirl phase of a zoom-whirl orbit I find that Ω decreases by $\approx 0.06\frac{q^2}{Mm}$. Due to the smallness of the ratio $\frac{q^2}{Mm}$ this change is tiny for one orbit, however since it accumulates over the inspiral, its effect on the total phase shift during the full inspiral can be of order unity. This statement is not directly transferable to the gravitational case since the radius r_0 of the orbit is not a gauge invariant quantity. Therefore I cannot distinguish between changes in Ω due to effects of the self-force and due to gauge choices. To obtain a meaningful measure of the effect of the gravitational self-force I need to compare two gauge invariant quantities, e.g. Ω and the gauge invariant u_t of [22].

I investigated the retardation of the self-force with respect to the motion of the particle. I found that the retardation is very weak for the r component of the force and strong in the t and φ components, which are linked to radiated energy and angular momentum. In the later cases the retardation is compatible with a delay of $\Delta t \approx 2(r_0(t) - R_{\rm delay})$, where $R_{\rm delay}$ is a constant depending on the particle's orbit.

Acknowledgments

I thank Eric Poisson and Steve Detweiler for useful discussions and suggestions. I gratefully acknowledge support by the Natural Sciences and Engineering Council of Canada. This work was supported in part by NSF grants PHY-0903973 and PHY-0904015. This work was made possible by the facilities of the Shared Hierarchical Academic Research Computing Network (SHARCNET:`www.sharcnet.ca`) as well as the e FoRCE cluster at Georgia Tech.

Appendix A: Translation tables

I require coupling coefficients to translate between the tensor harmonic modes of the Faraday tensor and the scalar harmonic modes of the tetrad components of the Faraday tensor.

As a first step, I reconstruct the Faraday tensor modes from the numerical variables. For the even mode auxiliary fields ψ, χ and ξ this reconstruction can be done algebraically while the odd sector requires a numerical differentiation of the numerical variable $\tilde{v}$. The reconstruction relations were already displayed in Eqs. (2.9) – (2.12), which involves both the even and odd modes.

In terms of the vector potential the Faraday tensor modes are reconstructed using the defining equation Eq. (2.1). In this case, the reconstruction of the Faraday tensor reads

$$F_{tr} = \sum_{\ell,m} (A^{\ell m}_{r,t} - A^{\ell m}_{t,r})\, Y^{\ell m}, \tag{A1a}$$

$$F_{tA} = \sum_{\ell,m} [(v^{\ell m}_{,t} - A^{\ell m}_{t})\, Z^{\ell m}_{A} + \tilde{v}^{\ell m}_{,t}\, X^{\ell m}_{A}], \tag{A1b}$$

$$F_{rA} = \sum_{\ell,m} [(v^{\ell m}_{,r} - A^{\ell m}_{r})\, Z^{\ell m}_{A} + \tilde{v}^{\ell m}_{,r}\, X^{\ell m}_{A}], \tag{A1c}$$

$$F_{\theta\varphi} = \sum_{\ell,m} \tilde{v}_{\ell m}\, (X^{\ell m}_{\varphi,\theta} - X^{\ell m}_{\theta,\varphi}). \tag{A1d}$$

Clearly both the expansion Eqs. (2.9) – (2.12) and the one in Eqs. (A1a) – (A1d) are of the same form and it is only necessary to obtain one set of translation coefficients to handle both the calculation using ψ, χ and ξ in the main text and the one using the vector potential that will be presented in appendix C.

The tetrad components $F_{(\mu)(\nu)}$ are decomposed in terms of scalar spherical harmonics

$$F_{(\mu)(\nu)} = \sum_{\ell,m} F^{\ell m}_{(\mu)(\nu)} Y_{\ell m}, \tag{A2}$$

where each mode is given by

$$F^{\ell m}_{(\mu)(\nu)} = \int F_{(\mu)(\nu)} \bar{Y}_{\ell m}\, {\rm d}\Omega. \tag{A3}$$

To obtain expressions for the coupling coefficients I substitute $F_{(\mu)(\nu)} = F_{\alpha\beta} e^{\alpha}{}_{(\mu)} e^{\beta}{}_{(\nu)}$ into Eq. (A3)

$$\begin{aligned}
F^{\ell m}_{(\mu)(\nu)} &= \int \mathrm{d}\Omega\, F_{(\mu)(\nu)} \bar{Y}^{\ell m} \\
&= \int \mathrm{d}\Omega\, \left(A_{\beta,\alpha} - A_{\alpha,\beta}\right) e^{\alpha}{}_{(\mu)} e^{\beta}{}_{(\nu)} \bar{Y}^{\ell m} \\
&= \int \sum_{\ell',m'} \Big[\left(A_{b,a} - A_{a,b}\right) e^{a}{}_{(\mu)} e^{b}{}_{(\nu)} \bar{Y}^{\ell m} \\
&\quad + \left(A_{b,A} - A_{A,b}\right) e^{A}{}_{(\mu)} e^{b}{}_{(\nu)} \bar{Y}^{\ell m} \\
&\quad + \left(A_{B,a} - A_{a,B}\right) e^{a}{}_{(\mu)} e^{B}{}_{(\nu)} \bar{Y}^{\ell m} \\
&\quad + \left(A_{B,A} - A_{A,B}\right) e^{A}{}_{(\mu)} e^{B}{}_{(\nu)} \bar{Y}^{\ell m} \Big] \mathrm{d}\Omega \\
&\equiv \sum_{\ell',m'} \Big[C^{ab}_{(\mu)(\nu)}(\ell' m'|\ell m) \left(A^{\ell' m'}_{b,a} - A^{\ell' m'}_{a,b} \right) \\
&\quad + D^{a}_{(\mu)(\nu)}(\ell' m'|\ell m) \left(\partial_a v^{\ell' m'} - A^{\ell' m'}_{a} \right) \\
&\quad + E^{a}_{(\mu)(\nu)}(\ell' m'|\ell m) \partial_a \tilde{v}^{\ell' m'} \\
&\quad + E_{(\mu)(\nu)}(\ell' m'|\ell m) \tilde{v}^{\ell' m'} \Big],
\end{aligned} \tag{A4}$$

which defines the coupling coefficients. It is often possible to express these coupling coefficients in terms of linear combinations of the coupling coefficients derived in paper I for the scalar field.

To simplify the notation of the coupling coefficients I use

$$\gamma^{\ell m} = \sqrt{\frac{(\ell+m)(\ell+m+1)}{(2\ell+1)(2\ell+3)}}, \tag{A5}$$

$$\epsilon^{\ell m} = \sqrt{\frac{(\ell+m+1)(\ell-m+1)}{(2\ell+1)(2\ell+3)}}, \tag{A6}$$

as shorthands for recurring combinations of terms. With these the reusable scalar coupling coefficients are written as

$$\begin{aligned}
C^{r}_{(+)}(\ell' m'|\ell m) &= -\gamma^{\ell-1,m} \sqrt{f} \delta_{\ell' \ell-1} \delta_{m' m-1} \\
&\quad + \gamma^{\ell,-m+1} \sqrt{f} \delta_{\ell' \ell+1} \delta_{m' m-1}
\end{aligned} \tag{A7}$$

$$\begin{aligned}
C_{(+)}(\ell' m'|\ell m) &= \gamma^{\ell-1,m} \frac{\ell-1}{r} \delta_{\ell' \ell-1} \delta_{m' m-1} \\
&\quad + \gamma^{\ell,-m+1} \frac{\ell+2}{r} \delta_{\ell' \ell+1} \delta_{m' m-1},
\end{aligned} \tag{A8}$$

$$\begin{aligned}
C_{(-)}(\ell' m'|\ell m) &= -\gamma^{\ell-1,-m} \frac{\ell-1}{r} \delta_{\ell' \ell-1} \delta_{m' m+1} \\
&\quad - \gamma^{\ell,m+1} \frac{\ell+2}{r} \delta_{\ell' \ell+1} \delta_{m' m+1}.
\end{aligned} \tag{A9}$$

Similarly it proves useful to define lower order coupling coefficients for the odd sector, which is absent in the scalar case.

$$E_{(+)}(\ell' m'|\ell m) = -\frac{i}{r} \sqrt{(\ell-m+1)(\ell+m)} \delta_{\ell' \ell} \delta_{m' m-1}, \tag{A10}$$

$$E_{(-)}(\ell' m'|\ell m) = -\frac{i}{r} \sqrt{(\ell+m+1)(\ell-m)} \delta_{\ell' \ell} \delta_{m' m+1}. \tag{A11}$$

In terms of the scalar coupling coefficients, the first coefficient for the expansion of $F_{(0)(+)}$ is given by

$$\begin{aligned}
C^{tr}_{(0)(+)}(\ell' m'|\ell m) &= \int Y^{\ell' m'} e^{t}_{(0)} e^{r}_{(+)} \bar{Y}^{\ell m} \mathrm{d}\Omega \\
&= \frac{1}{\sqrt{f}} \int Y^{\ell' m'} e^{r}_{(+)} \bar{Y}^{\ell m} \mathrm{d}\Omega \\
&= C^{r}_{(+)}(\ell' m'|\ell m)/\sqrt{f},
\end{aligned} \tag{A12}$$

and all other combinations of a, b and (μ), (ν) lead to vanishing $C^{ab}_{(\mu)(\nu)}$. Similarly for the remaining non-vanishing coefficients for the $F_{(0)(+)}$ component

$$D^{t}_{(0)(+)}(\ell' m'|\ell m) = C_{(+)}(\ell' m'|\ell m)/\sqrt{f}, \tag{A13}$$

$$E^{t}_{(0)(+)}(\ell' m'|\ell m) = E_{(+)}(\ell' m'|\ell m)/\sqrt{f}. \tag{A14}$$

The coupling coefficients for $F_{(+)(-)}$ contain both even and odd modes. The first non-vanishing one is $D^{r}_{(+)(-)}(\ell' m'|\ell m)$, which is given by

$$\begin{aligned}
D^{r}_{(+)(-)}(\ell' m'|\ell m) &= \sqrt{f} \gamma^{\ell,-m+1} C_{(-)}(\ell' m'|\ell+1, m-1) \\
&\quad - \sqrt{f} \gamma^{\ell-1,m} C_{(-)}(\ell' m'|\ell-1, m-1) \\
&\quad + \sqrt{f} \gamma^{\ell,m+1} C_{(+)}(\ell' m'|\ell+1, m+1) \\
&\quad - \sqrt{f} \gamma^{\ell-1,-m} C_{(+)}(\ell' m'|\ell-1, m+1),
\end{aligned} \tag{A15}$$

while the coefficients coupling to odd modes are

$$\begin{aligned}
E^{r}_{(+)(-)}(\ell' m'|\ell m) &= \sqrt{f} \gamma^{\ell,-m+1} E_{(-)}(\ell' m'|\ell+1, m-1) \\
&\quad - \sqrt{f} \gamma^{\ell-1,m} E_{(-)}(\ell' m'|\ell-1, m-1) \\
&\quad + \sqrt{f} \gamma^{\ell,m+1} E_{(+)}(\ell' m'|\ell+1, m+1) \\
&\quad - \sqrt{f} \gamma^{\ell-1,-m} E_{(+)}(\ell' m'|\ell-1, m+1),
\end{aligned} \tag{A16}$$

$$\begin{aligned}
E_{(+)(-)}(\ell' m'|\ell m) &= -2i/r^2 (\ell+1)(\ell+2) \epsilon^{\ell m} \delta_{\ell' \ell+1} \delta_{m' m} \\
&\quad - 2i/r^2 (\ell-1) \ell \epsilon^{\ell-1,m} \delta_{\ell' \ell-1} \delta_{m' m}.
\end{aligned} \tag{A17}$$

Appendix B: Regularization parameters

I mimic the treatment in paper I and start from the covariant expression for the singular vector potential tensor

in Eq. (464) of [23]

$$\nabla_\beta A^S_\alpha(x) = -\frac{q}{2r^2}U_{\alpha\beta'}u^{\beta'}\nabla_\beta r - \frac{q}{2r^2_{\rm adv}}U_{\alpha\beta''}u^{\beta''}\nabla_\beta r_{\rm adv} + \frac{q}{2r}U_{\alpha\beta';\beta}u^{\beta'} + \frac{q}{2r}U_{\alpha\beta';\gamma'}u^{\beta'}u^{\gamma'}\nabla_\beta u + \frac{q}{2r_{\rm adv}}U_{\alpha\beta'';\beta}u^{\beta''} + \frac{q}{2r_{\rm adv}}U_{\alpha\beta'';\gamma''}u^{\beta''}u^{\gamma''}\nabla_\beta v + \frac{1}{2}qV_{\alpha\beta'}u^{\beta'}\nabla_\beta u - \frac{1}{2}qV_{\alpha\beta''}u^{\beta''}\nabla_\beta v - \frac{1}{2}q\int_u^v \nabla_\beta V_{\alpha\mu}(x,z(\tau))u^\beta(\tau)\,{\rm d}\tau. \tag{B1}$$

I have introduced a large number of symbols. x is the point where the field is evaluated, x' and x'' are the retarded and advanced points of x on the world line $z(\tau)$. They are connected to x with unique future-directed and past-directed null geodesics, respectively. $u(x)$ and $v(x)$ are the retarded and advanced time functions such that $x' = z(\tau = u)$, $x'' = z(\tau = v)$. $u^{\alpha'}$ and $u^{\alpha''}$ are the four velocity at x' and x'' respectively. Further I define Synge's world function $\sigma(x,\bar{x})$ which is numerically equal to half the squared geodesic distance between two points x and $\bar{x}$. Using its gradient $\sigma_\alpha = \nabla_\alpha\sigma(x,\bar{x})$, I define $r = u^{\alpha'}\sigma_{\alpha'}(x,x')$ and $r_{\rm adv} = -u^{\alpha''}\sigma_{\alpha''}(x,x'')$, the affine parameter distances of x away from the world line along its future/past light cone. The potentials U and V appearing in Eq. (B1) are the direct and tail parts of the retarded Green function $G_{\alpha\bar{\beta}}(x,\bar{x})$ associated with the wave operator.

From the definition of r, $r_{\rm adv}$, u, and v it follows that (see Section 3.3.3 of [23])

$$\nabla_\alpha u = -\sigma_\alpha(x,x')/r, \tag{B2}$$
$$\nabla_\alpha v = \sigma_\alpha(x,x'')/r_{\rm adv}, \tag{B3}$$
$$\nabla_\alpha r = -\sigma_{\alpha'\beta'}u^{\alpha'}u^{\beta'}\nabla_\alpha u + \sigma_{\alpha'\alpha}u^{\alpha'}, \tag{B4}$$
$$\nabla_\alpha r_{\rm adv} = -\sigma_{\alpha''\beta''}u^{\alpha''}u^{\beta''}\nabla_\alpha u - \sigma_{\alpha''\alpha}u^{\alpha''}, \tag{B5}$$

which are valid for geodesic motion.

The potentials $U_{\alpha\beta'}$, $U_{\alpha\beta''}$ are determined by Eq. (322) of [23]

$$U_\alpha{}^{\beta'} = g^{\beta'}{}_\alpha\Delta^{1/2}(x,x'), \tag{B6}$$
$$U_\alpha{}^{\beta''} = g^{\beta''}{}_\alpha\Delta^{1/2}(x,x''), \tag{B7}$$

where $g^{\bar{\mu}}{}_\nu$ is the parallel propagator from x^ν to $\bar{x}^\mu$ and $\Delta \equiv \det(-g^{\alpha'}{}_\alpha\sigma^\alpha_{;\beta'})$ is the van Vleck determinant. Of the potentials $V_{\alpha\beta'}$ and $V_{\alpha\beta''}$ appearing in Eq. (B1) I only need to know the scaling behaviour following from Eq. (320) of [23]:

$$V_{\alpha\beta'} = O(\varepsilon^2), \tag{B8}$$
$$V_{\alpha\beta''} = O(\varepsilon^2), \tag{B9}$$
$$\nabla_\beta V_{\alpha\mu} = O(\varepsilon). \tag{B10}$$

These expressions are valid in vacuum spacetimes where the Ricci tensor vanishes.

Again mirroring the calculation in paper I, I introduce the arbitrary point $\bar{x} \equiv z(\bar{\tau})$ on the world line and expand the quantities in Eq. (B1) in terms of a Taylor expansion around $\bar{x}$. I introduce the convenient quantities

$$\bar{r} \equiv \sigma_{\bar{\alpha}}(x,\bar{x})u^{\bar{\alpha}}, \tag{B11}$$
$$s^2 \equiv (g^{\bar{\alpha}\bar{\beta}} + u^{\bar{\alpha}}u^{\bar{\beta}})\sigma_{\bar{\alpha}}(x,\bar{x})\sigma_{\bar{\beta}}(x,\bar{x}), \tag{B12}$$

together with the time differences

$$\Delta_+ \equiv v - \bar{\tau}, \qquad \Delta_- \equiv u - \bar{\tau} \tag{B13}$$

from the advanced (retarded) point to the reference point $\bar{x}$.

I also use the expansion of the derivatives of the parallel propagator around the point $\bar{x}$

$$g^{\bar{\alpha}}{}_{\beta;\bar{\gamma}} = -g^{\bar{\beta}}{}_\beta\left(\frac{1}{2}R^{\bar{\alpha}}{}_{\bar{\beta}\bar{\gamma}\bar{\delta}}\sigma^{\bar{\delta}} - \frac{1}{6}R^{\bar{\alpha}}{}_{\bar{\beta}\bar{\gamma}\bar{\delta};\bar{\varepsilon}}\sigma^{\bar{\delta}}\sigma^{\bar{\varepsilon}}\right) + O(\varepsilon^3), \tag{B14}$$

$$g^{\bar{\alpha}}{}_{\beta;\gamma} = -g^{\bar{\beta}}{}_\beta g^{\bar{\gamma}}{}_\gamma\left(\frac{1}{2}R^{\bar{\alpha}}{}_{\bar{\beta}\bar{\gamma}\bar{\delta}}\sigma^{\bar{\delta}} - \frac{1}{3}R^{\bar{\alpha}}{}_{\bar{\beta}\bar{\gamma}\bar{\delta};\bar{\varepsilon}}\sigma^{\bar{\delta}}\sigma^{\bar{\varepsilon}}\right) + O(\varepsilon^3), \tag{B15}$$

as well as an expansion for the second derivative of Synge's world function

$$\sigma_{\bar{\alpha}\bar{\beta}} = g_{\bar{\alpha}\bar{\beta}} - \frac{1}{3}R_{\bar{\alpha}\bar{\gamma}\bar{\beta}\bar{\delta}}\sigma^{\bar{\gamma}}\sigma^{\bar{\delta}} + \frac{1}{12}R_{\bar{\alpha}\bar{\gamma}\bar{\beta}\bar{\delta};\bar{\varepsilon}}\sigma^{\bar{\gamma}}\sigma^{\bar{\delta}}\sigma^{\bar{\varepsilon}} + O(\varepsilon^4), \tag{B16}$$

and the van Vleck determinant

$$\Delta^{1/2} = 1 + O(\epsilon^4), \tag{B17}$$

which I calculate using the methods described in Sec. (2.4.2) of [23].

I make use of the fact that the bi-tensors

$$U_\alpha(\tau) \equiv U_{\alpha\mu}u^\mu, \tag{B18}$$
$$U_{\alpha\beta}(\tau) \equiv U_{\alpha\mu;\beta}u^\mu, \text{ and} \tag{B19}$$
$$\dot{U}_\alpha(\tau) \equiv U_{\alpha\mu;\nu}u^\mu u^\nu \tag{B20}$$

appearing in Eq. (B1) do not bear a free index on the world line, making them scalars on the world line. With w being either u or v and $\Delta \equiv w - \bar{\tau} = \Delta_\mp$ I expand these as

$$U_\alpha(w) = U_\alpha + \dot{U}_\alpha\Delta + \frac{1}{2}\ddot{U}_\alpha\Delta^2 + \frac{1}{6}U^{(3)}_\alpha\Delta^3 + O(\varepsilon^4), \tag{B21}$$

$$U_{\alpha\beta}(w) = U_{\alpha\beta} + \dot{U}_{\alpha\beta}\Delta + \frac{1}{2}\ddot{U}_{\alpha\beta}\Delta^2 + O(\varepsilon^3), \text{ and} \tag{B22}$$

$$\dot{U}_\alpha(w) = \dot{U}_\alpha + \ddot{U}_\alpha\Delta + \frac{1}{2}U^{(3)}_\alpha\Delta^2 + O(\varepsilon^3), \tag{B23}$$

where it is understood that the coefficient functions are evaluated at $\tau = \bar{\tau}$.

Repeatedly taking derivatives of Eq. (B7) and contracting with $u^{\bar\mu}$ I find for the first set of coefficients

$$U_\alpha = g^{\bar\alpha}{}_\alpha u_{\bar\alpha} + O(\varepsilon^4), \tag{B24}$$

$$\dot U_\alpha = g^{\bar\alpha}{}_\alpha \left(\frac{1}{2}R_{\bar\alpha uu\sigma} - \frac{1}{6}R_{\bar\alpha uu\sigma|\sigma}\right) + O(\varepsilon^3), \tag{B25}$$

$$\ddot U_\alpha = \frac{1}{3}g^{\bar\alpha}{}_\alpha R_{\bar\alpha uu\sigma|u} + O(\varepsilon^2), \tag{B26}$$

$$U^{(3)}_\alpha = 0 + O(\varepsilon), \tag{B27}$$

where I have introduced the notation $R_{\bar\alpha uu\sigma} \equiv R_{\bar\alpha\bar\beta\bar\gamma\bar\delta}u^{\bar\beta}u^{\bar\gamma}\sigma^{\bar\delta}$ and $R_{\bar\alpha uu\sigma|\sigma} \equiv R_{\bar\alpha\bar\beta\bar\gamma\bar\delta;\bar\varepsilon}u^{\bar\beta}u^{\bar\gamma}\sigma^{\bar\delta}\sigma^{\bar\varepsilon}$; I will use this notation and its natural extension to higher derivatives and different combinations of $u^{\bar\mu}$ and $\sigma^{\bar\mu}$ frequently below.

Similarly I find for the second set

$$U_{\alpha\beta} = g^{\bar\alpha}{}_\alpha g^{\bar\beta}{}_\beta \left(\frac{1}{2}R_{\bar\alpha u\bar\beta\sigma} - \frac{1}{3}R_{\bar\alpha u\bar\beta\sigma|\sigma}\right) + O(\varepsilon^3), \tag{B28}$$

$$\dot U_{\alpha\beta} = g^{\bar\alpha}{}_\alpha g^{\bar\beta}{}_\beta \left(\frac{1}{2}R_{\bar\alpha u\bar\beta u} + \frac{1}{6}R_{\bar\alpha u\bar\beta\sigma|u} - \frac{1}{3}R_{\bar\alpha u\bar\beta u|\sigma}\right) + O(\varepsilon^2), \tag{B29}$$

$$\ddot U_{\alpha\beta} = \frac{1}{3}g^{\bar\alpha}{}_\alpha g^{\bar\beta}{}_\beta R_{\bar\alpha u\bar\beta u|u} + O(\varepsilon). \tag{B30}$$

Note that the third set does not involve new coefficients, but only those already calculated for U_α.

Finally I copy expressions for $\Delta_\pm$, r, $r_{\rm adv}$, u, v and their gradients from paper I

$$\Delta_\pm = (\bar r \pm s) \mp \frac{(\bar r \pm s)^2}{6s}R_{u\sigma u\sigma} \mp \frac{(\bar r \pm s)^2}{24s}\left[(\bar r \pm s)R_{u\sigma u\sigma|u} - R_{u\sigma u\sigma|\sigma}\right] + O(\varepsilon^5), \tag{B31}$$

$$r = s - \frac{\bar r^2 - s^2}{6s}R_{u\sigma u\sigma} - \frac{\bar r - s}{24s}\left[(\bar r - s)(\bar r + 2s)R_{u\sigma u\sigma|u} - (\bar r + s)R_{u\sigma u\sigma|\sigma}\right] + O(\varepsilon^5), \tag{B32}$$

$$r_{\rm adv} = s - \frac{\bar r^2 - s^2}{6s}R_{u\sigma u\sigma} - \frac{\bar r + s}{24s}\left[(\bar r + s)(\bar r - 2s)R_{u\sigma u\sigma|u} - (\bar r - s)R_{u\sigma u\sigma|\sigma}\right] + O(\varepsilon^5), \tag{B33}$$

$$\begin{aligned}\nabla_\alpha u = \frac{1}{s}g^{\bar\alpha}{}_\alpha\Bigg\{&[\sigma_{\bar\alpha} + (\bar r - s)u_{\bar\alpha}]\\ &+ \left[\frac{1}{6}(\bar r - s)R_{\bar\alpha\sigma u\sigma} - \frac{1}{3}(\bar r - s)^2R_{\bar\alpha u\sigma u} + \frac{\bar r^2 - s^2}{6s^2}R_{u\sigma u\sigma}\sigma_{\bar\alpha} + \frac{(\bar r - s)^2(\bar r + 2s)}{6s^2}R_{\sigma u\sigma u|u}u_{\bar\alpha}\right]\\ &+ \Bigg[-\frac{1}{12}(\bar r - s)R_{\bar\alpha u\sigma u|\sigma} + \frac{1}{8}(\bar r - s)^2R_{\bar\alpha u\sigma u|\sigma} + \frac{1}{24}(\bar r - s)^2R_{\bar\alpha\sigma u\sigma|u} - \frac{1}{12}(\bar r - s)^3R_{\bar\alpha u\sigma u|u}\\ &+ \frac{\bar r - s}{24s^2}\left((\bar r - s)(\bar r + 2s)R_{u\sigma u\sigma|u} - (\bar r + s)R_{u\sigma u\sigma|\sigma}\right)\sigma_{\bar\alpha}\\ &+ \frac{(\bar r - s)^2}{24s^2}\left((\bar r - s)(\bar r + 3s)R_{u\sigma u\sigma|\sigma} - (\bar r + 2s)R_{u\sigma u\sigma|\sigma}\right)u_{\bar\alpha}\Bigg] + O(\varepsilon^5)\Bigg\},\end{aligned} \tag{B34}$$

$$\begin{aligned}\nabla_\alpha v = -\frac{1}{s}g^{\bar\alpha}{}_\alpha\Bigg\{&[\sigma_{\bar\alpha} + (\bar r + s)u_{\bar\alpha}]\\ &+ \left[\frac{1}{6}(\bar r + s)R_{\bar\alpha\sigma u\sigma} - \frac{1}{3}(\bar r + s)^2R_{\bar\alpha u\sigma u} + \frac{\bar r^2 - s^2}{6s^2}R_{u\sigma u\sigma}\sigma_{\bar\alpha} + \frac{(\bar r + s)^2(\bar r - 2s)}{6s^2}R_{\sigma u\sigma u|u}u_{\bar\alpha}\right]\\ &+ \Bigg[-\frac{1}{12}(\bar r + s)R_{\bar\alpha u\sigma u|\sigma} + \frac{1}{8}(\bar r + s)^2R_{\bar\alpha u\sigma u|\sigma} + \frac{1}{24}(\bar r + s)^2R_{\bar\alpha\sigma u\sigma|u} - \frac{1}{12}(\bar r + s)^3R_{\bar\alpha u\sigma u|u}\\ &+ \frac{\bar r + s}{24s^2}\left((\bar r + s)(\bar r - 2s)R_{u\sigma u\sigma|u} - (\bar r - s)R_{u\sigma u\sigma|\sigma}\right)\sigma_{\bar\alpha}\\ &+ \frac{(\bar r + s)^2}{24s^2}\left((\bar r + s)(\bar r - 3s)R_{u\sigma u\sigma|\sigma} - (\bar r - 2s)R_{u\sigma u\sigma|\sigma}\right)u_{\bar\alpha}\Bigg] + O(\varepsilon^5)\Bigg\},\end{aligned} \tag{B35}$$

$$\nabla_\alpha r = -\frac{1}{s} g^{\bar\alpha}{}_\alpha \left\{ [\sigma_{\bar\alpha} + \bar r u_{\bar\alpha}] + \left[\frac{1}{6}\bar r R_{\bar\alpha\sigma u\sigma} - \frac{1}{3}(\bar r^2 - s^2) R_{\bar\alpha u\sigma u} + \frac{\bar r^2 + s^2}{6s^2} R_{u\sigma u\sigma}\sigma_{\bar\alpha} + \frac{\bar r(\bar r^2 - s^2)}{6s^2} R_{u\sigma u\sigma} u_{\bar\alpha} \right] \right.$$
$$+ \left[-\frac{1}{12}\bar r R_{\bar\alpha\sigma u\sigma|\sigma} + \frac{1}{8}(\bar r^2 - s^2) R_{\bar\alpha u\sigma u|\sigma} + \frac{1}{24}(\bar r^2 - s^2) R_{\bar\alpha\sigma u\sigma|u} \right.$$
$$- \frac{1}{12}(\bar r - s)^2(\bar r + 2s) R_{\bar\alpha u\sigma u|u} + \frac{1}{24s^2}\left((\bar r - s)(\bar r^2 + \bar r s + 4s^2) R_{u\sigma u\sigma|u} - (\bar r^2 + s^2) R_{u\sigma u\sigma|\sigma}\right)\sigma_{\bar\alpha}$$
$$\left. \left. + \frac{\bar r - s}{24s^2}\left((\bar r - s)(\bar r^2 + 2\bar r s + 3s^2) R_{u\sigma u\sigma|u} - \bar r(\bar r + s) R_{u\sigma u\sigma|\sigma}\right) u_{\bar\alpha} \right] + O(\epsilon^5) \right\}, \tag{B36}$$

$$\nabla_\alpha r_{\rm adv} = -\frac{1}{s} g^{\bar\alpha}{}_\alpha \left\{ [\sigma_{\bar\alpha} + \bar r u_{\bar\alpha}] + \left[\frac{1}{6}\bar r R_{\bar\alpha\sigma u\sigma} - \frac{1}{3}(\bar r^2 - s^2) R_{\bar\alpha u\sigma u} + \frac{\bar r^2 + s^2}{6s^2} R_{u\sigma u\sigma}\sigma_{\bar\alpha} + \frac{\bar r(\bar r^2 - s^2)}{6s^2} R_{u\sigma u\sigma} u_{\bar\alpha} \right] \right.$$
$$+ \left[-\frac{1}{12}\bar r R_{\bar\alpha\sigma u\sigma|\sigma} + \frac{1}{8}(\bar r^2 - s^2) R_{\bar\alpha u\sigma u|\sigma} + \frac{1}{24}(\bar r^2 - s^2) R_{\bar\alpha\sigma u\sigma|u} \right.$$
$$- \frac{1}{12}(\bar r + s)^2(\bar r - 2s) R_{\bar\alpha u\sigma u|u} + \frac{1}{24s^2}\left((\bar r + s)(\bar r^2 - \bar r s + 4s^2) R_{u\sigma u\sigma|u} - (\bar r^2 + s^2) R_{u\sigma u\sigma|\sigma}\right)\sigma_{\bar\alpha}$$
$$\left. \left. + \frac{\bar r + s}{24s^2}\left((\bar r + s)(\bar r^2 - 2\bar r s + 3s^2) R_{u\sigma u\sigma|u} - \bar r(\bar r - s) R_{u\sigma u\sigma|\sigma}\right) u_{\bar\alpha} \right] + O(\epsilon^5) \right\}. \tag{B37}$$

After substituting Eqs. (B2) – (B37) into Eq. (B1) (all of them) and sorting out the orders I find the final expression for the covariant expansion of $A^S_{\alpha;\beta}$

$$A^S_{\alpha;\beta} = q g^{\bar\alpha}{}_\alpha g^{\bar\beta}{}_\beta \left\{ \left[\frac{1}{s^3} u_{\bar\alpha}\sigma_{\bar\beta} + \frac{\bar r}{s^3} u_{\bar\alpha} u_{\bar\beta} \right] + \left[\frac{\bar r}{6s^3} u_{\bar\alpha} R_{\bar\beta\sigma u\sigma} + \left(\frac{\bar r}{2s^3}\sigma_{\bar\beta} + \frac{\bar r^2 - s^2}{2s^3} u_{\bar\beta} \right) R_{\bar\alpha uu\sigma} \right.$$
$$+ \frac{\bar r^2 - s^2}{3s^2} u_{\bar\alpha} R_{\bar\beta uu\sigma} + \frac{1}{2s} R_{\bar\alpha u\bar\beta\sigma} + \frac{3\bar r^2 - s^2}{6s^5} R_{u\sigma u\sigma} u_{\bar\alpha}\sigma_{\bar\beta} + \frac{\bar r(\bar r^2 - s^2)}{2s^5} R_{u\sigma u\sigma} u_{\bar\alpha} u_{\bar\beta} + \frac{\bar r}{2s} R_{\bar\alpha u\bar\beta u} \left. \right]$$
$$+ \left[-\frac{\bar r}{12s^3} u_{\bar\alpha} R_{\bar\beta\sigma u\sigma|\sigma} - \frac{\bar r^2 - s^2}{24s^3} u_{\bar\alpha} R_{\bar\beta\sigma\sigma u|u} - \left(\frac{\bar r}{6s^3}\sigma_{\bar\beta} + \frac{\bar r^2 - s^2}{6s^3} u_{\bar\beta} \right) R_{\bar\alpha uu\sigma|\sigma} - \frac{\bar r^2 - s^2}{8s^3} u_{\bar\alpha} R_{\bar\beta uu\sigma|\sigma} \right.$$
$$- \frac{1}{3s^2} R_{\bar\alpha u\bar\beta\sigma|\sigma} + \left(\frac{\bar r^2 - s^2}{6s^3}\sigma_{\bar\beta} + \frac{\bar r(\bar r^2 - 3s^2)}{6s^3} u_{\bar\beta} \right) R_{\bar\alpha uu\sigma|u} + \frac{\bar r(\bar r^2 - 3s^2)}{12s^3} u_{\bar\alpha} R_{\bar\beta uu\sigma|u} - \frac{\bar r}{3s} R_{\bar\alpha u\bar\beta u|\sigma}$$
$$+ \frac{\bar r}{6s} R_{\bar\alpha u\bar\beta\sigma|u} + \frac{\bar r^2 + s^2}{6s^3} R_{\bar\alpha u\bar\beta u|u} + \left(-\frac{3\bar r^2 - s^2}{24s^5} R_{u\sigma u\sigma|\sigma} + \frac{\bar r(\bar r^2 - s^2)}{8s^5} R_{u\sigma u\sigma|u} \right) u_{\bar\alpha}\sigma_{\bar\beta}$$
$$\left. \left. + \left(-\frac{\bar r(\bar r^2 - s^2)}{8s^5} R_{u\sigma u\sigma|\sigma} + \frac{(\bar r^2 - s^2)^2}{8s^5} R_{u\sigma u\sigma|u} \right) u_{\bar\alpha} u_{\bar\beta} \right] \right\} + O(\varepsilon^2), \tag{B38}$$

where terms in square brackets are of the same power in ε.

I copy the results for the coordinate expansion of $\sigma_{\bar\alpha}(x,\bar x)$ and $g^{\bar\alpha}{}_\beta(x,\bar x)$ from Eqs. (3.16) – (3.19) and Eqs. (3.30) – (3.33) of paper I. I use

$$-\sigma_{\bar\alpha}(x,\bar x) = g_{\alpha\beta} w^\beta + A_{\alpha\beta\gamma} w^\beta w^\gamma + A_{\alpha\beta\gamma\delta} w^\beta w^\gamma w^\delta + A_{\alpha\beta\gamma\delta\varepsilon} w^\beta w^\gamma w^\delta w^\varepsilon + O(\varepsilon^5), \tag{B39}$$

$$A^\alpha{}_{\beta\gamma} \equiv \frac{1}{2}\Gamma^\alpha{}_{\beta\gamma}, \tag{B40}$$

$$A^\alpha{}_{\beta\gamma\delta} \equiv \frac{1}{6}\left(\Gamma^\alpha{}_{\beta\gamma,\delta} + \Gamma^\alpha{}_{\beta\mu}\Gamma^\mu{}_{\gamma\delta}\right), \tag{B41}$$

$$A^\alpha{}_{\beta\gamma\delta\epsilon} \equiv \frac{1}{24}\left(\Gamma^\alpha{}_{\beta\gamma,\delta\epsilon} + \Gamma^\alpha{}_{\beta\gamma,\mu}\Gamma^\mu{}_{\delta\epsilon} + 2\Gamma^\alpha{}_{\beta\mu}\Gamma^\mu{}_{\gamma\delta,\epsilon} + \Gamma^\alpha{}_{\mu\nu}\Gamma^\mu{}_{\beta\gamma}\Gamma^\nu{}_{\delta\epsilon}\right), \tag{B42}$$

as well as

$$g^{\bar\mu}{}_\alpha(x,\bar x) = \delta^\mu{}_\alpha + B^\mu{}_{\alpha\beta} w^\beta + B^\mu{}_{\alpha\beta\gamma} w^\beta w^\gamma + B^\mu{}_{\alpha\beta\gamma\delta} w^\beta w^\gamma w^\delta + O(\varepsilon^4),, \tag{B43}$$

$$B^\mu{}_{\alpha\beta} \equiv \Gamma^\mu{}_{\alpha\beta}, \tag{B44}$$

$$B^\mu{}_{\alpha\beta\gamma} \equiv \frac{1}{2}\left(\Gamma^\mu{}_{\alpha\beta,\gamma} + \Gamma^\mu{}_{\beta\nu}\Gamma^\nu{}_{\alpha\gamma}\right), \tag{B45}$$

$$B^{\mu}{}_{\alpha\beta\gamma\delta} \equiv \frac{1}{12}\Big(2\Gamma^{\mu}{}_{\alpha\beta,\gamma\delta} + 2\Gamma^{\nu}{}_{\alpha\beta}\Gamma^{\mu}{}_{\nu\gamma,\delta} - \Gamma^{\nu}{}_{\beta\gamma}\Gamma^{\mu}{}_{\alpha\nu,\delta} + 4\Gamma^{\mu}{}_{\beta\nu}\Gamma^{\nu}{}_{\alpha\gamma,\delta} + \Gamma^{\nu}{}_{\beta\gamma}\Gamma^{\mu}{}_{\alpha\delta,\nu} - \Gamma^{\mu}{}_{\beta\nu}\Gamma^{\nu}{}_{\alpha\lambda}\Gamma^{\lambda}{}_{\gamma\delta} + \Gamma^{\mu}{}_{\nu\lambda}\Gamma^{\nu}{}_{\alpha\beta}\Gamma^{\lambda}{}_{\gamma\delta} + 2\Gamma^{\mu}{}_{\beta\nu}\Gamma^{\nu}{}_{\gamma\lambda}\Gamma^{\lambda}{}_{\alpha\delta}\Big), \quad \text{(B46)}$$

where $w^{\alpha} \equiv x^{\alpha} - x^{\bar{\alpha}}$ is the coordinate distance between x and $\bar{x}$. Together with Eq. (B38) these equations form an expansion in w^{α} of the singular part of the gradient of the vector potential around a point x near the world line of the particle. I finally calculate the tetrad components of the singular Faraday tensor as

$$F^{S}_{(\mu)(\nu)} = (A^{S}_{\beta,\alpha} - A^{S}_{\alpha,\beta})e^{\alpha}{}_{(\mu)}e^{\beta}{}_{(\nu)}. \quad \text{(B47)}$$

From this point on I proceed exactly as described in Section V of paper I using MAPLE and GRTENSORII to perform the calculations. I find, after an extremely tedious calculation,

$$A_{(0)(+)} = \mathrm{sign}(\Delta)\Big[\frac{i\dot{r}_0 J}{r_0 \mathfrak{f} a^2} - \frac{1}{r_0^2}\Big]e^{i\varphi_0}, \quad \text{(B48)}$$

$$B_{(0)(+)} = \Big\{\Big[-\frac{iE(J^2-r_0^2)\dot{r}_0}{a^3\pi\mathfrak{f}J} + \frac{E(2-\mathfrak{f})}{\pi\mathfrak{f}ar_0}\Big]\mathcal{E} - \frac{ir_0^2 E\dot{r}_0}{a^3 J\mathfrak{f}\pi}\mathcal{K}\Big\}e^{i\varphi_0}, \quad \text{(B49)}$$

$$\begin{aligned} D_{(0)(+)} = \Bigg\{ & \Bigg[\frac{iEr_0^2(-14r_0^2J^2 + J^4 + r_0^4)\dot{r}_0^3}{8\pi J\mathfrak{f}a^7} - \frac{(-r_0\mathfrak{f}J^2 + 2r_0J^2 + 7r_0^3\mathfrak{f} - 14r_0^3)E\dot{r}_0^2}{8a^5\mathfrak{f}\pi} \\ & + i\frac{\big(8MJ^8 - 14MJ^6r_0^2 - 3r_0^5J^4 - 80MJ^4r_0^4 + 4J^4r_0^5\mathfrak{f} - 7r_0^7J^2 - 68Mr_0^6J^2 + 4r_0^9 - 26Mr_0^8 - 4r_0^9\mathfrak{f}\big)E\dot{r}_0}{8r_0^5a^5\mathfrak{f}J\pi} \\ & - \frac{(8Mr_0\mathfrak{f}J^6 - 8r_0^3MJ^4 + 38J^4r_0^3\mathfrak{f} - 2r_0^6J^2 - 16Mr_0^5J^2 + 3J^2r_0^6\mathfrak{f} + 54J^2r_0^5\mathfrak{f} + 20r_0^7\mathfrak{f} + 5r_0^8\mathfrak{f} - 6r_0^8)E}{8r_0^7a^3\mathfrak{f}\pi}\Bigg]\mathcal{E} \\ & + \Bigg[\frac{iEr_0^4(7J^2 - r_0^2)\dot{r}_0^3}{8\pi J\mathfrak{f}a^7} - \frac{(2-\mathfrak{f})r_0^3E\dot{r}_0^2}{2a^5\mathfrak{f}\pi} \\ & + \frac{\big(4Mr_0\mathfrak{f}J^4 + 20J^2r_0^3\mathfrak{f} + 8Mr_0^3J^2 + 14r_0^5M\mathfrak{f} - 2r_0^6 + 12Mr_0^5 + r_0^6\mathfrak{f}\big)E}{8r_0^5a^3\mathfrak{f}\pi} \\ & - \frac{i(2MJ^6 - 9Mr_0^2J^4 - 2J^2r_0^5\mathfrak{f} - 20Mr_0^4J^2 - 2r_0^7\mathfrak{f} + 2r_0^7 - 13Mr_0^6)E\dot{r}_0}{4r_0^3a^5\mathfrak{f}J\pi}\Bigg]\mathcal{K}\Bigg\}e^{i\varphi_0}, \end{aligned} \quad \text{(B50)}$$

$$A_{(+)(-)} = \mathrm{sign}(\Delta)\frac{2iEJ}{a^2r_0\mathfrak{f}}e^{i\varphi_0}, \quad \text{(B51)}$$

$$B_{(+)(-)} = -2i\Bigg\{\Big[-\frac{(r_0^2-J^2)\dot{r}_0^2}{a^3\pi J\mathfrak{f}} + \frac{-J^2r_0\mathfrak{f} + 2r_0J^2 + 2r_0^3 - 2r_0^3\mathfrak{f}}{r_0^3aJ\pi}\Big]\mathcal{E} + \Big[\frac{r_0^2\dot{r}_0^2}{a^3\mathfrak{f}J\pi} - \frac{2(1-\mathfrak{f})}{aJ\pi}\Big]\mathcal{K}\Bigg\}e^{i\varphi_0}, \quad \text{(B52)}$$

$$\begin{aligned} D_{(+)(-)} = -2i\Bigg\{ & \Big[-\frac{r_0^2(-14r_0^2J^2 + J^4 + r_0^4)\dot{r}_0^4}{8\mathfrak{f}\pi Ja^7} - \Big(4M\mathfrak{f}J^8 - 7Mr_0^2\mathfrak{f}J^6 + 2J^4r_0^5\mathfrak{f} + 2J^4r_0^4M - J^4r_0^5 \\ & - 43J^4r_0^4\mathfrak{f}M - 7J^2r_0^7\mathfrak{f} - 27J^2Mr_0^6\mathfrak{f} - 11Mr_0^8\mathfrak{f} - r_0^9\mathfrak{f} + r_0^9 - 2r_0^8M\Big)r_0^{1/2}\dot{r}_0^2\Big/\Big(4r_0^5a^5J\mathfrak{f}\pi\Big) \\ & - \Big(8M\mathfrak{f}J^8 - 8J^6Mr_0^2 + 30Mr_0^2\mathfrak{f}J^6 - 2J^4r_0^5 + 10J^4r_0^4\mathfrak{f}M - 24J^4r_0^4M + 3J^4r_0^5\mathfrak{f} \\ & - 28J^2Mr_0^6 + J^2r_0^7\mathfrak{f} - 28J^2Mr_0^6\mathfrak{f} - 20Mr_0^8\mathfrak{f} - 12r_0^8M\Big)\Big/\Big(8r_0^7a^3J\pi\Big)\Big]\mathcal{E} \\ & + \Big[-\frac{r_0^4(7J^2 - r_0^2)\dot{r}_0^4}{8\mathfrak{f}\pi Ja^7} \\ & + \frac{4M\mathfrak{f}J^6 - 16J^4Mr_0^2 + 4r_0^2\mathfrak{f}MJ^4 - 18J^2r_0^4\mathfrak{f}M - 28J^2r_0^4M - J^2\mathfrak{f}r_0^5 - 12r_0^6M - 20r_0^6\mathfrak{f}M}{8r_0^5a^3J\pi} \\ & + \Big(2M\mathfrak{f}J^6 - 9r_0^2\mathfrak{f}MJ^4 + J^2r_0^5 - 2J^2r_0^4M - 5J^2\mathfrak{f}r_0^5 - 14J^2r_0^4\mathfrak{f}M - 2r_0^6M + r_0^7 \\ & - 11r_0^6\mathfrak{f}M - \mathfrak{f}r_0^7\Big)\dot{r}_0^2\Big/\Big(4r_0^{5/2}a^5J\mathfrak{f}\pi\Big)\Big]\mathcal{K}\Bigg\}e^{i\varphi_0}, \end{aligned} \quad \text{(B53)}$$

where $\mathfrak{f} = \sqrt{\frac{r_0-2M}{r_0}}$, $a^2 = r_0^2 + J^2$.

Here, the rescaled elliptic integrals $\mathcal{E}$ and $\mathcal{K}$ are defined by

$$\mathcal{E} \equiv \frac{2}{\pi}\int_0^{\pi/2}(1-k\sin^2\psi)^{1/2}\,\mathrm{d}\psi = F\left(-\frac{1}{2},\frac{1}{2};1;k\right), \tag{B54}$$

and

$$\mathcal{K} \equiv \frac{2}{\pi}\int_0^{\pi/2}(1-k\sin^2\psi)^{-1/2}\,\mathrm{d}\psi = F\left(\frac{1}{2},\frac{1}{2};1;k\right), \tag{B55}$$

in which $F(a,b;c;x)$ are the hypergeometric functions and $k \equiv J^2/(r_0^2+J^2)$.

Appendix C: Vector potential calculation

In this section I describe a variant of the numerical calculation discussed in the main part of the paper that uses the vector potential instead of the Faraday tensor. To this end I decompose the vector potential and the sources in terms of vectorial spherical harmonics

$$A_a(t,r^*,\theta,\phi) = \tfrac{1}{r}A_a^{\ell m}(t,r^*)Y_{\ell m}(\theta,\phi), \tag{C1a}$$

$$j_a(t,r^*,\theta,\phi) = j_a^{\ell m}(t,r^*)Y_{\ell m}(\theta,\phi) \qquad \text{for } a = t, r^*, \tag{C1b}$$

$$A_A(t,r^*,\theta,\phi) = v_{\ell m}(t,r^*)Z_A^{\ell m}(\theta,\phi) + \tilde{v}_{\ell m}(t,r^*)X_A^{\ell m}(\theta,\phi), \tag{C1c}$$

$$j_A(t,r^*,\theta,\phi) = j_{\ell m}^{\text{even}}(t,r^*)Z_A^{\ell m}(\theta,\phi) + j_{\ell m}^{\text{odd}}(t,r^*)X_A^{\ell m}(\theta,\phi) \quad \text{for } A = \theta,\phi, \tag{C1d}$$

and substitute this into the Maxwell equations for the vector potential in the Lorenz gauge $g^{\alpha\beta}A_{\alpha;\beta} = 0$:

$$g^{\mu\nu}A_{\alpha;\mu\nu} - R^{\beta}{}_{\alpha}A^{\beta} = -4\pi j_\alpha, \tag{C2}$$

where $R_{\alpha\beta}$ is the spacetime's Ricci tensor, which vanishes in Schwarzschild spacetime. Substituting Eq. (C1) into Eq. (C2) I arrive at two decoupled sets of equations for the even ($A_a^{\ell m}$, $v_{\ell m}$) and odd ($\tilde{v}_{\ell m}$) modes

$$-\frac{\partial^2 A_t^{\ell m}}{\partial t^2} + \frac{\partial^2 A_t^{\ell m}}{\partial r^{*2}} + \frac{2M}{r^2}\left(\frac{\partial A_{r^*}^{\ell m}}{\partial t} - \frac{\partial A_t^{\ell m}}{\partial r^*}\right) - VA_t^{\ell m} = -4\pi r f j_t^{\ell m}, \tag{C3}$$

$$-\frac{\partial^2 A_{r^*}^{\ell m}}{\partial t^2} + \frac{\partial^2 A_{r^*}^{\ell m}}{\partial r^{*2}} + \frac{2M}{r^2}\left(\frac{\partial A_t^{\ell m}}{\partial t} - \frac{\partial A_{r^*}^{\ell m}}{\partial r^*}\right) - \left(V + 2\frac{f^2}{r^2}\right)A_{r^*}^{\ell m} + fVv_{\ell m} = -4\pi r f j_{r^*}^{\ell m}, \tag{C4}$$

$$-\frac{\partial^2 v_{\ell m}}{\partial t^2} + \frac{\partial^2 v_{\ell m}}{\partial r^{*2}} - Vv_{\ell m} + 2\frac{f}{r^2}A_{r^*}^{\ell m} = -4\pi f j_{\ell m}^{\text{even}}, \tag{C5}$$

$$-\frac{\partial^2 \tilde{v}_{\ell m}}{\partial t^2} + \frac{\partial^2 \tilde{v}_{\ell m}}{\partial r^{*2}} - V\tilde{v}_{\ell m} = -4\pi f j_{\ell m}^{\text{odd}}, \tag{C6}$$

where V and $j_\alpha^{\ell m}$ is defined as in Eqs. (2.15b) and (2.4) in the main text.

1. Numerical method

I discretize the set of reduced equations Eqs. (C3) – (C6) using Lousto's method as described in section II of the main text. Since the source terms on the right hand side are less singular for the vector potential than they are for the Faraday tensor, I do not have to distinguish between sourced and vacuum cells in the integral over the potential terms.

Terms containing first derivatives $\frac{\partial\psi}{\partial t}$, $\frac{\partial\psi}{\partial r^*}$, where now and in the remainder of the appendix ψ stands for any of $A_t^{\ell m}$, $A_{r^*}^{\ell m}$, $v^{\ell m}$ or $\tilde{v}^{\ell m}$, were not treated in [10], but, for generic vacuum cells, can be handled in a straightforward manner

$$\iint_{\text{cell}}\mathrm{d}u\,\mathrm{d}v\,V(r)\frac{\partial\psi}{\partial t} = 2h(\psi_3-\psi_2)V_0 + O(h^4), \tag{C7}$$

$$\iint_{\text{cell}}\mathrm{d}u\,\mathrm{d}v\,V(r)\frac{\partial\psi}{\partial r^*} = 2h(\psi_4-\psi_1)V_0 + O(h^4). \tag{C8}$$

This fails for cells traversed by the particle, since the field is only continuous across the world line but not differentiable. For these cells I take recourse to Lousto's original

algorithm, which has to deal with a similar issue, and use

$$\iint_{\text{cell}} \mathrm{d}u\,\mathrm{d}v\, V(r)\frac{\partial\psi}{\partial t} = V_0 \sum_i A_i \partial_t \psi_i + O(h^3), \tag{C9}$$

$$\iint_{\text{cell}} \mathrm{d}u\,\mathrm{d}v\, V(r)\frac{\partial\psi}{\partial r^*} = V_0 \sum_i A_i \partial_{r^*} \psi_i + O(h^3), \tag{C10}$$

where $A_1,\ldots,A_4$ are the subareas indicated in Fig. 3 and $\partial_t\psi_1$, …, $\partial_t\psi_4$, $\partial_{r^*}\psi_1$, …, $\partial_{r^*}\psi_4$ are zeroth order accurate approximations to the derivatives in the subareas. I calculate these using grid points outside of the cell on the same side of the world line as the corresponding subarea, e.g.

$$\partial_{r^*}\psi_1 = \frac{\psi(t, r^* - h) - \psi(t, r^* - 3h)}{2h} + O(h). \tag{C11}$$

2. Gauge condition

In contrast to the scalar field, the electromagnetic vector potential has to satisfy a gauge condition

$$Z \equiv g^{\alpha\beta} A_{\alpha;\beta} = 0. \tag{C12}$$

Analytically the gauge condition is preserved by the evolution equations, so that it is sufficient to impose it on the initial data. Numerically, however, small violations of the gauge condition due to the numerical approximation can be amplified exponentially and come to dominate the numerical data. To handle this situation I introduce a gauge damping scheme as described in [24, 25]. That is I add a term of the form

$$\frac{4M}{r^2} Z = \frac{4M}{r^2}\left(-\frac{1}{r-2M}\frac{\partial A_t}{\partial t} + \frac{1}{r-2M}\frac{\partial A_{r^*}}{\partial r^*} + \frac{1}{r^2}A_{r^*} - \frac{\ell(\ell+1)}{r^2} v\right) \tag{C13}$$

to the t components of the evolution equations Eqs. (C2), which dampens out violations of the gauge condition. This choice proved to be numerically stable for the radiative ($\ell > 0$) modes but unstable for the monopole ($\ell = 0$) mode.

3. Monopole mode

The monopole moment of an electromagnetic field is non-radiative. This makes its behaviour sufficiently different from that of the radiative ($\ell > 0$) modes that the approach outlined earlier fails for $\ell = 0$. In this case Eq. (C2) reduces to a set of coupled equations for $A_a^{0,0}$ only. Rather than solving the system of equations directly for $A_t^{0,0}$ and $A_{r^*}^{0,0}$ I use the analytical result for the F_{tr} component of the Faraday tensor derived in section II C in the main part of the paper. This proves to be sufficient to reconstruct the combination $A_{r,t}^{0,0} - A_{t,r}^{0,0}$ appearing in Eq. (A4).

4. Initial values and boundary conditions

I handle the problem of initial data and boundary conditions the same way as in the main text, that is I arbitrarily choose the fields to vanish on the characteristic slices $u = u_0$ and $v = v_0$

$$A_\alpha(u = u_0) = A_\alpha(v = v_0) = 0, \tag{C14}$$

thereby adding a certain amount of spurious waves to the solution which show up as an initial burst. Gauge violations in this initial data are damped out along with those arising during the evolution.

I implement ingoing wave boundary conditions near the event horizon and choose a numerical domain that covers the full domain of dependence of the initial data near the outer boundary.

5. Extraction of the field data at the particle

In order to extract the value of the fields and their first derivatives at the position of the particle, I use a variant of the extraction scheme described in paper II. I introduce a piecewise polynomial

$$p(x) = \begin{cases} c_0 + c_1 x + \frac{c_3}{2}x^2 & \text{if } x < 0 \\ c_0' + c_1' x + \frac{c_3}{2}x^2 & \text{if } x > 0 \end{cases} \tag{C15}$$

in $x \equiv r^* - r_0^*$ on the current slice. Its coefficients to the left and right of the world line are linked by jump conditions $c_n = c_n' + [\partial_{r^*}^n \psi]$ listed in Appendix D 2. Fitting this polynomial to the three grid points closest to the particle, I extract approximations for $\psi(t_0, r_0^*)$ and $\frac{\partial\psi(t_0,r_0^*)}{\partial r^*}$ which are just the coefficients c_0, c_1 respectively. Once I have obtained these, I proceed as in section V of the main part of the paper following [14] to obtain values for $\frac{\partial\psi(t_0,r_0^*)}{\partial t}$.

6. Results

Using the vector potential code described above I can reproduce the results obtained from the Faraday tensor method discussed in the main paper. The differences are small, typically of the order of $10^{-3}\%$ of the field values as shown in Fig. 20. I expect the Faraday tensor code to yield more accurate results since the costly numerical differentiation that is necessary in the vector potential calculation is absent. Nevertheless I can reproduce e.g. the correct decay behaviour of the multipole coefficients for a zoom-whirl orbit as shown in Fig. 21.

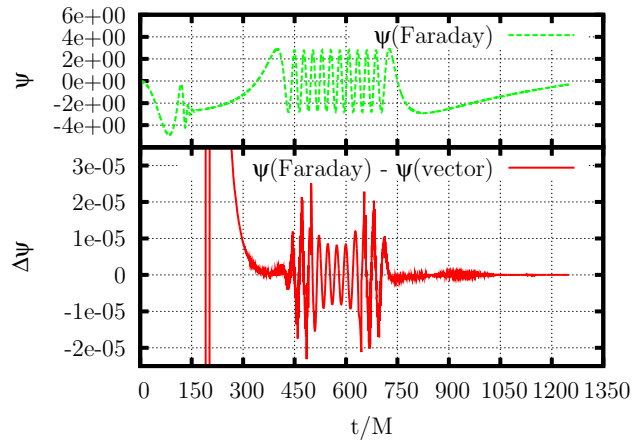

FIG. 20: Differences between $F^{\ell m}_{tr}$ calculated using the vector potential and calculated using the Faraday tensor method for $\ell = 2$, $m = 2$ mode of field for the zoom-whirl orbit shown in Fig. 8. Displayed are the difference and the actual field. The stepsizes were $h = 1.041\bar{6} \times 10^{-2}\,M$ and $h = 1/512\,M$ for the vector potential calculation and the Faraday tensor calculation respectively.

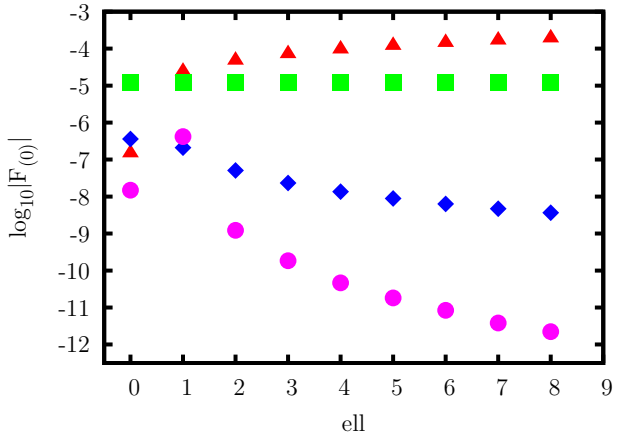

FIG. 21: Multipole coefficients of $\frac{M^2}{q}\,\mathrm{Re}\,F^R_{(0)}$ for a particle on a zoom-whirl orbit ($p = 7.8001$, $e = 0.9$), calculated using a stepsize of $h = 0.125M$ for the $\ell = 1$ modes and increasing the resolution linearly with ℓ for $\ell > 1$. The coefficients are extracted at $t = 1100\,M$ when the particle is deep within the zoom phase. Red triangles are used for the unregularized multipole coefficients $F_{(0),\ell}$, squares, diamonds and disks are used for the partly regularized coefficients after the removal of the $A_{(0)}$, $B_{(0)}$ and $D_{(0)}$ terms respectively.

Appendix D: Jump conditions

1. Faraday tensor calculation

Since the source term in Eqs. (2.15b) – (2.15f) contains a term proportional to $\delta'(r^* - r^*_0)$, the field is discontinuous across the world line of the particle. I use

$$[\partial_t^n \partial_{r^*}^m \psi] = \lim_{\varepsilon\to 0^+} [\partial_t^n \partial_{r^*}^m \psi(t_0, r^*_0 + \varepsilon) - \partial_t^n \partial_{r^*}^m \psi(t_0, r^*_0 - \varepsilon)] \quad \text{(D1)}$$

to denote the jump in $\partial_t^n \partial_{r^*}^m \psi$ across the world line. I only calculate jump conditions in the r^* direction up to $[\partial_{r^*}\psi]$, which I find by substituting the ansatz

$$\psi = \psi_<(t, r^*)\theta(r^*_0 - r^*) + \psi_>(t, r^*)\theta(r^* - r^*_0) \quad \text{(D2)}$$

into Eqs. (2.15b) – (2.15f) and its t and r^* derivatives. Demanding in each step that the singularity structure on the left hand side matches that of the sources (and their derivatives) on the right hand side yields the jump conditions

$$[\psi] = \frac{F_\psi}{f_0[(\partial_t r^*_0)^2 - 1]}, \quad \text{(D3)}$$

and

$$[\partial_{r^*}\psi] = -\frac{G_\psi}{(\partial_t r^*_0)^2 - 1} - \frac{\partial_t^2 r^*_0 \left[3\,(\partial_t r^*_0)^2 + 1\right] F_\psi}{f_0\,[(\partial_t r^*_0)^2 - 1]^3} + 2\frac{\partial_t r^*_0\,\partial_t\,(F_\psi/f_0)}{[(\partial_t r^*_0)^2 - 1]^2}, \quad \text{(D4)}$$

where ψ stands for either one of ψ, χ, or ξ.

2. Vector potential calculation

Since the source term in Eq. (C2) is singular, the field is only continuous across the world line of the particle, but not smooth. I use

$$[\partial_t^n \partial_{r^*}^m \psi] = \lim_{\varepsilon\to 0^+} [\partial_t^n \partial_{r^*}^m \psi(t_0, r^*_0 + \varepsilon) - \partial_t^n \partial_{r^*}^m \psi(t_0, r^*_0 - \varepsilon)] \quad \text{(D5)}$$

to denote the jump in $\partial_t^n \partial_{r^*}^m \psi$ across the world line. For my purposes I only need the jump conditions in the r^* direction up to $\left[\partial_{r^*}^2 \psi\right]$, which I find by substituting the ansatz

$$A^{\ell m}_a(t, r^*) = A^{\ell m}_{a,<}(t, r^*)\theta(r^*_0 - r^*) + A^{\ell m}_{a,>}(t, r^*)\theta(r^* - r^*_0), \quad \text{(D6)}$$

$$v^{\ell m}(t, r^*) = v^{\ell m}_<(t, r^*)\theta(r^*_0 - r^*) + v^{\ell m}_>(t, r^*)\theta(r^* - r^*_0), \quad \text{(D7)}$$

$$\tilde{v}^{\ell m}(t, r^*) = \tilde{v}^{\ell m}_<(t, r^*)\theta(r^*_0 - r^*) + \tilde{v}^{\ell m}_>(t, r^*)\theta(r^* - r^*_0) \quad \text{(D8)}$$

into Eqs. (C3) – (C6) and its t and r^* derivatives. Demanding in each step that the singularity structure on the left hand side matches that of the sources (and their

derivatives) on the right hand side yields the jump conditions

$$\left[A_a^{\ell m}\right] = \left[w^{\ell m}\right] = 0, \tag{D9}$$

$$\left[\partial_{r^*} A_a^{\ell m}\right] = \frac{E^2}{E^2 - \dot{r}_0^2} S_a, \tag{D10}$$

$$\left[\partial_{r^*} w^{\ell m}\right] = \frac{E^2}{E^2 - \dot{r}_0^2} S_{\text{even/odd}}, \tag{D11}$$

$$\left[\partial_{r^*}^2 A_a^{\ell m}\right] = \left(\frac{2ME^4}{r_0^2(E^2-\dot{r}_0^2)^2} - f_0\frac{(3\dot{r}_0^2+E^2)E^2\ddot{r}_0}{(E^2-\dot{r}_0^2)^3}\right) S_a + \frac{2ME^3\dot{r}_0}{r_0^2(E^2-\dot{r}_0^2)^2} S_b - f_0\frac{2E^2\dot{r}_0}{(E^2-\dot{r}_0^2)^2}\dot{S}_a, \tag{D12}$$

$$\left[\partial_{r^*}^2 w^{\ell m}\right] = -f_0\frac{(3\dot{r}_0^2+E^2)E^2\ddot{r}_0}{(E^2-\dot{r}_0^2)^3} S_{\text{even/odd}} - f_0\frac{2E^2\dot{r}_0}{(E^2-\dot{r}_0^2)^2}\dot{S}_{\text{even/odd}}, \tag{D13}$$

where $a, b \in \{t, r^*\}, a \neq b$, $w \in \{v, \tilde{v}\}$.

[1] R. Haas, Phys. Rev. D **75**, 124011 (2007), 0704.0797.

[2] R. Haas and E. Poisson, Phys. Rev. D **74**, 044009 (pages 29) (2006), gr-qc/0605077, URL http://link.aps.org/abstract/PRD/v74/e044009.

[3] L. Barack and A. Ori, Phys. Rev. D **61**, 061502 (2000), gr-qc/9912010.

[4] I. Vega and S. Detweiler, Phys. Rev. D **77**, 084008 (2008), 0712.4405.

[5] L. Barack, D. A. Golbourn, and N. Sago, Phys. Rev. **D76**, 124036 (2007), 0709.4588.

[6] A. Pound and E. Poisson, Phys. Rev. D **77**, 044012 (2008), 0708.3037.

[7] L. Barack and N. Sago, Phys. Rev. **D83**, 084023 (2011), 1101.3331.

[8] N. Warburton, S. Akcay, L. Barack, J. R. Gair, and N. Sago (2011), * Temporary entry *, 1111.6908.

[9] C. W. Misner, K. S. Thorne, and J. A. Wheeler, *Gravitation* (W. H. Freeman, San Francisco, 1973), ISBN 0716703343.

[10] C. O. Lousto and R. H. Price, Phys. Rev. D **56**, 6439 (1997), gr-qc/9705071.

[11] T. Regge, Phys. Rev. **108**, 1063 (1957).

[12] K. Martel and E. Poisson, Phys. Rev. D **71**, 104003 (2005), gr-qc/0502028.

[13] C. T. Cunningham and R. H. Price, The Astrophysical Journal **230**, 870 (1979).

[14] N. Sago, talk in 10th Capra meeting at UAH (2007).

[15] S. Detweiler, E. Messaritaki, and B. F. Whiting, Phys. Rev. D **67**, 104016 (2003), gr-qc/0205079.

[16] L. M. Diaz-Rivera, E. Messaritaki, B. F. Whiting, and S. Detweiler, Physical Review D (Particles, Fields, Gravitation, and Cosmology) **70**, 124018 (pages 14) (2004), gr-qc/0410011, URL http://link.aps.org/abstract/PRD/v70/e124018.

[17] S. L. Detweiler, Phys. Rev. **D77**, 124026 (2008), 0804.3529.

[18] N. Sago, L. Barack, and S. L. Detweiler, Phys. Rev. **D78**, 124024 (2008), 0810.2530.

[19] L. Barack and N. Sago, Phys. Rev. Lett. **102**, 191101 (2009), 0902.0573.

[20] M. J. Pfenning and E. Poisson, Phys. Rev. D **65**, 084001 (2002), gr-qc/0012057.

[21] C. DeWitt-Morette and B. S. Dewitt, *Relativite, groups et topologie = Relativity, groups and topology : lectures delivered at les Houches during the 1963 session of the Summer School of* (Gordon and Breach, New York, 1964).

[22] S. Detweiler, Phys. Rev. D **77**, 124026 (2008), 0804.3529.

[23] E. Poisson, Living Reviews in Relativity **7** (2004), URL http://www.livingreviews.org/lrr-2004-6.

[24] C. Gundlach, J. M. Martin-Garcia, G. Calabrese, and I. Hinder, Class. Quant. Grav. **22**, 3767 (2005), gr-qc/0504114.

[25] L. Barack and C. O. Lousto, Phys. Rev. D **72**, 104026 (2005), gr-qc/0510019.